

1    **Patient-specific Boolean models of signalling**  
2    **networks guide personalised treatments**

3    Arnau Montagud<sup>1,2,3,4,\*</sup>, Jonas Béal<sup>1,2,3</sup>, Luis Tobalina<sup>5,\$</sup>, Pauline Traynard<sup>1,2,3</sup>, Vigneshwari  
4    Subramanian<sup>5,§</sup>, Bence Szalai<sup>5,6</sup>, Róbert Alföldi<sup>7</sup>, László Puskás<sup>7</sup>, Alfonso Valencia<sup>4,8</sup>,  
5    Emmanuel Barillot<sup>1,2,3</sup>, Julio Saez-Rodriguez<sup>5,9,#</sup>, Laurence Calzone<sup>1,2,3,\*,#</sup>

6

7    1 Institut Curie, PSL Research University, Paris, France

8    2 INSERM, U900, Paris, France

9    3 MINES ParisTech, PSL Research University, CBIO-Centre for Computational Biology,  
10   Paris, France

11   4 Barcelona Supercomputing Center (BSC), Barcelona, Spain

12   5 Faculty of Medicine, Joint Research Centre for Computational Biomedicine

13   (JRC-COMBINE), RWTH Aachen University, 52074 Aachen, Germany

14   6 Semmelweis University, Faculty of Medicine, Department of Physiology, Budapest,  
15   Hungary

16   7 Astridbio Technologies Ltd., 6728 Szeged, Hungary

17   8 Institució Catalana de Recerca i Estudis Avançats (ICREA), 08010, Barcelona, Spain

18   9 Faculty of Medicine and Heidelberg University Hospital, Institute of Computational  
19   Biomedicine, Heidelberg University, Heidelberg, Germany

20

21   \* corresponding authors: [arnau.montagud@bsc.es](mailto:arnau.montagud@bsc.es), [laurence.calzone@curie.fr](mailto:laurence.calzone@curie.fr)

22   # These authors contributed equally to this work and should be considered co-senior  
23   authors.

24   \$ Current address: Bioinformatics and Data Science, Research and Early Development,  
25   Oncology R&D, AstraZeneca, Cambridge, UK

26   § Current address: Data Science & Artificial Intelligence, Imaging & Data Analytics, Clinical  
27   Pharmacology & Safety Sciences, R&D, AstraZeneca, Gothenburg, Sweden

28   **Abstract**

29   Prostate cancer is the second most occurring cancer in men worldwide. To better  
30   understand the mechanisms of tumorigenesis and possible treatment responses, we  
31   developed a mathematical model of prostate cancer which considers the major signalling  
32   pathways known to be deregulated. We personalised this Boolean model to molecular data  
33   to reflect the heterogeneity and specific response to perturbations of cancer patients. 488  
34   prostate samples were used to build patient-specific models and compared to available  
35   clinical data. Additionally, eight prostate cell-line-specific models were built to validate our  
36   approach with dose-response data of several drugs. The effects of single and combined  
37   drugs were tested in these models under different growth conditions. We identified 15  
38   actionable points of interventions in one cell-line-specific model whose inactivation hinders  
39   tumorigenesis. To validate these results, we tested nine small molecule inhibitors of five of  
40   those putative targets and found a dose-dependent effect on four of them, notably those

41 targeting HSP90 and PI3K. These results highlight the predictive power of our personalised  
42 Boolean models and illustrate how they can be used for precision oncology.

## 43 Introduction

44 Like most cancers, prostate cancer arises from mutations in single somatic cells that induce  
45 deregulations in processes such as proliferation, invasion of adjacent tissues and  
46 metastasis. Not all prostate patients respond to the treatments in the same way, depending  
47 on the stage and type of their tumour (Chen and Zhou, 2016) and differences in their genetic  
48 and epigenetic profiles (Toth et al., 2019; Yang et al., 2018). The high heterogeneity of these  
49 profiles can be explained by a large number of interacting proteins and the complex cross-  
50 talks between the cell signalling pathways that can be altered in cancer cells. Because of  
51 this complexity, understanding the process of tumorigenesis and tumour growth would  
52 benefit from a systemic and dynamical description of the disease. At the molecular level, this  
53 can be tackled by a simplified mechanistic cell-wide model of protein interactions of the  
54 underlying pathways, dependent on external environmental signals.

55 Although continuous mathematical modelling has been widely used to study cellular  
56 biochemistry dynamics (e.g., ordinary differential equations) (Goldbeter, 2002; Kholodenko  
57 et al., 1995; Le Novère, 2015; Sible and Tyson, 2007; Tyson et al., 2019), this formalism  
58 does not scale up well to large signalling networks, due to the difficulty of estimating kinetic  
59 parameter values (Babtie and Stumpf, 2017). In contrast, the logical (or logic) modelling  
60 formalism represents a simpler means of abstraction where the causal relationships between  
61 proteins (or genes) are encoded with logic statements, and dynamical behaviours are  
62 represented by transitions between discrete states of the system (Kauffman, 1969; Thomas,  
63 1973). In particular, Boolean models, the simplest implementation of logical models,  
64 describe each protein as a binary variable (ON/OFF). This framework is flexible, requires in  
65 principle no quantitative information, can be hence applied to large networks combining  
66 multiple pathways, and can also provide a qualitative understanding of molecular systems  
67 lacking detailed mechanistic information.

68 In the last years, logical and, in particular, Boolean modelling has successfully been used to  
69 describe the dynamics of human cellular signal transduction and gene regulations (Calzone  
70 et al., 2010; Cho et al., 2016; Flobak et al., 2015; Grieco et al., 2013; Helikar et al., 2008;  
71 Traynard et al., 2016) and their deregulation in cancer (Fumiā and Martins, 2013; Hu et al.,  
72 2015). Numerous applications of logical modelling have shown that this framework is able to  
73 delineate the main dynamical properties of complex biological regulatory networks (Abou-  
74 Jaoudé et al., 2011; Faure et al., 2006).

75 However, the Boolean approach is purely qualitative and does not consider the real time of  
76 cellular events (half time of proteins, triggering of apoptosis, etc.). To cope with this issue,  
77 we developed the MaBoSS software to compute continuous Markov Chain simulations on  
78 the model state transition graph (STG), in which a model state is defined as a vector of  
79 nodes that are either active or inactive. In practice, MaBoSS associates transition rates for  
80 activation and inhibition of each node of the network, enabling it to account for different time  
81 scales of the processes described by the model. Given some initial conditions, MaBoSS  
82 applies a Monte-Carlo kinetic algorithm (or Gillespie algorithm) to the STG to produce time  
83 trajectories (Stoll et al., 2017, 2012) such that time evolution of the model state probabilities

84 can be estimated. Stochastic simulations can easily explore the model dynamics with  
85 different initial conditions by varying the probability of having a node active at the beginning  
86 of the simulations and by modifying the model such that it accounts for genetic and  
87 environmental perturbations (e.g., presence or absence of growth factors, or death  
88 receptors). For each case, the effect on the probabilities of selected read-outs can be  
89 measured (Cohen et al., 2015; Montagud et al., 2017).

90 When summarising the biological knowledge into a network and translating it into logical  
91 terms, the obtained model is generic and cannot explain the differences and heterogeneity  
92 between patients' responses to treatments. Models can be trained with dedicated  
93 perturbation experiments (Dorier et al., 2016; Saez-Rodriguez et al., 2009), but such data  
94 can only be obtained with non-standard procedures such as microfluidics from patients'  
95 material (Eduati et al., 2020). To address this limitation, we developed a methodology to use  
96 different omics data that are more commonly available to personalise generic models to  
97 individual cancer patients or cell lines and verified that the obtained models correlated with  
98 clinical results such as patient survival information (Béal et al., 2019). In the present work,  
99 we apply this approach to prostate cancer to suggest targeted therapy to patients based on  
100 their omics profile (Figure 1). We first built 488 patient- and eight cell line-prostate-specific  
101 models using data from The Cancer Genome Atlas (TCGA) and the Genomics of Drug  
102 Sensitivity in Cancer (GDSC) projects, respectively. Simulating these models with the  
103 MaBoSS framework, we identified points of intervention that diminish the probability of  
104 reaching pro-tumorigenic phenotypes. Lastly, we developed a new methodology to simulate  
105 drug effects on these data-tailored Boolean models and present a list of viable drugs and  
106 regimes that could be used on these patient- and cell-line-specific models for optimal results.  
107 Experimental validations were performed on the LNCaP prostate cell line with two predicted  
108 targets, confirming the predictions of the model.

## 109 Results

### 110 Prostate Boolean model construction

111 A network of signalling pathways and genes relevant for prostate cancer progression was  
112 assembled to recapitulate the potential deregulations that lead to high-grade tumours.  
113 Dynamical properties were added onto this network to perform simulations, uncover  
114 therapeutic targets and explore drug combinations. The model was built upon a generic  
115 cancer Boolean model by Fumiā and Martins (2013), which integrates major signalling  
116 pathways and their substantial cross-talks. The pathways include the regulation of cell death  
117 and proliferation in many tumours.

118 This initial generic network was extended to include prostate-cancer-specific genes (e.g.,  
119 SPOP, AR, etc.), pathways identified using ROMA (Martignetti et al., 2016), OmniPath (Türei  
120 et al., 2021) and up-to-date literature. ROMA is applied on omics data, either transcriptomics  
121 or proteomics. In each pathway, the genes that contribute the most to the overdispersion are  
122 selected. ROMA was applied to the TCGA transcriptomics data using gene sets from cancer  
123 pathway databases (Appendix 1, Section 1.1.3, Appendix figure 1). These results were used  
124 as guidelines to extend the network to fully cover the alterations found in prostate cancer  
125 patients. OmniPath was used to complete our network finding connections between the

126 proteins of interest known to play a role in the prostate and the ones identified with ROMA,  
127 and the list of genes already present in the model (Appendix 1, Sections 1.1.3 and 1.1.4,  
128 Appendix figures 2 and 3). The final network includes pathways such as androgen receptor,  
129 MAPK, Wnt, NFkB, PI3K/AKT, MAPK, mTOR, SHH, the cell cycle, the epithelial-  
130 mesenchymal transition (EMT), apoptosis and DNA damage pathways.

131 This network was then converted into a Boolean model where all variables can take two  
132 values: 0 (inactivate or absent) or 1 (activate or present). Our model aims at predicting  
133 prostate phenotypic behaviours for healthy and cancer cells in different conditions. Nine  
134 inputs that represent some of these physiological conditions of interest were considered:  
135 Epithelial Growth Factor (EGF), Fibroblast Growth Factor (FGF), Transforming Growth  
136 Factor beta (TGFbeta), *Nutrients*, *Hypoxia*, *Acidosis*, *Androgen*, *Tumour Necrosis Factor*  
137 *alpha* (*TNF alpha*) and *Carcinogen*. These input nodes have no regulation. Their value is  
138 fixed according to the simulated experiment to represent the status of the  
139 microenvironmental characteristics (e.g., the presence or absence of growth factors, oxygen,  
140 etc.). A more complex multiscale approach would be required to consider the dynamical  
141 interaction with other cell types.

142 We defined six variables as output nodes that allow the integration of multiple phenotypic  
143 signals and simplify the analysis of the model. Two of these phenotypes represent the  
144 possible growth status of the cell: *Proliferation* and *Apoptosis*. *Apoptosis* is activated by  
145 Caspase 8 or Caspase 9, while *Proliferation* is activated by cyclins D and B (read-outs of the  
146 G1 and M phases, respectively). The *Proliferation* output is described in published models  
147 as specific stationary protein activation patterns, namely the following sequence of activation  
148 of cyclins: Cyclin D, then Cyclin E, then Cyclin A, and finally Cyclin B (Traynard et al., 2016).  
149 Here, we considered a proper sequence when Cyclin D activates first, allowing the release  
150 of the transcriptional factor E2F1 from the inhibitory complex it was forming with RB  
151 (retinoblastoma protein), and then triggering a series of events leading to the activation of  
152 Cyclin B, responsible for the cell's entry into mitosis (Appendix 1, Section 2.2, Appendix  
153 figure 5). We also define several phenotypic outputs that are readouts of cancer hallmarks:  
154 *Invasion*, *Migration*, (bone) *Metastasis* and *DNA repair*. The final model accounts for 133  
155 nodes and 449 edges (Figure 2, Supplementary File 1, and in GINsim format at the address:  
156 <http://ginsim.org/model/signalling-prostate-cancer>).

157

## 158 Prostate Boolean model simulation

159 The model can be considered as a model of healthy prostate cells when no mutants (or  
160 fused genes) are present. We refer to this model as the wild type model. These healthy cells  
161 mostly exhibit quiescence (neither proliferation nor apoptosis) in the absence of any input  
162 (Figure 3A). When *Nutrients* and growth factors (*EGF* or *FGF*) are present, *Proliferation* is  
163 activated (Figure 3B). *Androgen* is necessary for AR activation and helps in the activation of  
164 *Proliferation*, even though it is not necessary when *Nutrients* or growth factors are present.  
165 Cell death factors (such as Caspase 8 or 9) trigger *Apoptosis* in the absence of *SPOP*, while  
166 *Hypoxia* and *Carcinogen* facilitate apoptosis but are not necessary if cell death factors are  
167 present (Figure 3C).

168 In our model, the progression towards metastasis is described as a stepwise process.  
169 *Invasion* is first activated by known pro-invasive proteins: either  $\beta$ -catenin (Francis et al.,  
170 2013) or a combination of *CDH2* (De Wever et al., 2004), *SMAD* (Daroqui et al., 2012) or  
171 *EZH2* (Ren et al., 2012). *Migration* is then activated by *Invasion* and *EMT* and with either  
172 *AKT* or *AR* (Castoria et al., 2011). Lastly, (bone) *Metastasis* is activated by *Migration* and  
173 one of three nodes: *RUNX2* (Altieri et al., 2009), *ERG* (Adamo and Ladomery, 2016) or *ERG*  
174 fused with *TMPRSS2* (St John et al., 2012), *FLI1*, *ETV1* or *ETV4* (The Cancer Genome  
175 Atlas Research Network, 2015).

176 This prostate Boolean model was simulated stochastically using MaBoSS (Stoll et al., 2017,  
177 2012) and validated by recapitulating known phenotypes of prostate cells under  
178 physiological conditions (Figure 3 and Appendix 1, Sections 2.2 and 2.3, Appendix figures 5-  
179 7). In particular, we tested that combinations of inputs lead to non-aberrant phenotypes such  
180 as growth factors leading to apoptosis in wild type conditions; we also verified that the cell  
181 cycle events occur in proper order: as CyclinD gets activated, RB1 is phosphorylated and  
182 turned OFF, allowing E2F1 to mediate the synthesis of CyclinB (see Supplementary File 2  
183 for the jupyter notebook and the simulation of diverse cellular conditions).

## 184 Personalisation of the prostate Boolean model

### 185 Personalised TCGA prostate cancer patient Boolean models

186 We tailored the generic prostate Boolean model to a set of 488 TCGA prostate cancer  
187 patients (Appendix 1, Section 4, Appendix figure 9) using our personalisation method  
188 (PROFILE, (Béal et al., 2019)), constructing 488 individual Boolean models, one for each  
189 patient. Personalised models were built using three types of data: discrete data such as  
190 mutations and copy number alterations (CNA) and continuous data such as RNAseq data.  
191 For discrete data, the nodes corresponding to the mutations or the CNA were forced to 0 or  
192 1 according to the effect of alterations, based on *a priori* knowledge (i.e., if the mutation was  
193 reported to be activating or inhibiting the gene's activity). For continuous data, the  
194 personalisation method modifies the value for the transition rates of model variables and  
195 their initial conditions to influence the probability of some transitions. This corresponds, in a  
196 biologically-meaningful way, to translating genetic mutations as lasting modifications making  
197 the gene independent of regulation, and to translating RNA expression levels as modulation

198 of a signal but not changing the regulation rules (see Materials and Methods and in  
199 Appendix 1, Section 4.1, Appendix figure 10-14).

200 We assess the general behaviour of the individual patient-specific models by comparing the  
201 model outputs (i.e., probabilities to reach certain phenotypes) with clinical data. Here, the  
202 clinical data consist of a Gleason grade score associated with each patient, which in turn  
203 corresponds to the gravity of the tumour based on its appearance and the stage of invasion  
204 (Chen and Zhou, 2016; Gleason, 1992, 1977). We gathered output probabilities for all  
205 patient-specific models and confronted them to their Gleason scores. The phenotype  
206 *DNA\_repair*, which can be interpreted as a sensor of DNA damage and genome integrity  
207 which could lead to DNA repair, seems to separate low and high Gleason scores (Figure 4A  
208 and Appendix 1, Section 4.1, Appendix figures 15-18), confirming that DNA damage  
209 pathways are activated in patients (Marshall et al., 2019) but may not lead to the triggering of  
210 apoptosis in this model (Appendix 1, Section 4.1, Appendix figure 11). Also, the centroids of  
211 Gleason grades tend to move following *Proliferation*, *Migration* and *Invasion* variables. We  
212 then looked at the profiles of the phenotype scores across patients and their Gleason grade  
213 and found that the density of high *Proliferation* score (close to 1, Figure 4B) tends to  
214 increase as the Gleason score increases (from low to intermediate to high) and these  
215 distributions are significantly different (Kruskal-Wallis rank sum test, p-value=0.00207;  
216 Appendix 1, Section 4.1). The *Apoptosis* phenotype, however, does not have a clear trend  
217 across grades' probabilities (Figure 4C), even though the distributions are significantly  
218 different (Kruskal-Wallis rank sum test, p-value=2.83E-6; Appendix 1, Section 4.1).

## 219 Personalised drug predictions of TCGA Boolean models

220 Using the 488 TCGA-patient-specific models, we looked in each patient for genes that, when  
221 inhibited, hamper *Proliferation* or promote *Apoptosis* in the model. We focused on these  
222 inhibitions as most drugs interfere with the protein activity related to these genes, even  
223 though our methodology allows us to study increased protein activity related to over-  
224 expression of genes as well (Béal et al., 2019; Montagud et al., 2017). Interestingly, we  
225 found several genes that were found as suitable points of intervention in most of the patients  
226 (MYC\_MAX complex and SPOP were identified in more than 80% of the cases) (Appendix 1,  
227 Section 4.2, Appendix figure 19 and 20), but others were specific to only some of the  
228 patients (MXI1 was identified in only 4 patients, 1% of the total, GLI in only 7% and WNT in  
229 8% of patients). All the TCGA-specific personalised models can be found in Supplementary  
230 File 3, and the TCGA mutants and their phenotype scores can be found in Supplementary  
231 File 4.

232 Furthermore, we explored the possibility of finding combinations of treatments that could  
233 reduce the *Proliferation* phenotype or increase the *Apoptosis* one. To lower the  
234 computational power need, we narrowed down the list of potential candidates to a set of  
235 selected genes that are targets of already-developed drugs relevant in cancer progression  
236 (Table 1) and analysed the simulations of the models with all the single and combined  
237 perturbations.

238 We used the models to grade the effect that the combined treatments have in each one of  
239 the 488 TCGA-patient-specific models' phenotypes. This list of combinations of treatments  
240 can be used to compare the effects of drugs on each TCGA patient and allows us to propose

some of them for individual patients and to suggest drugs suitable to groups of patients (Supplementary File 4). Indeed, the inactivation of some of the targeted genes had a greater effect in some patients than in others, suggesting the possibility for the design of personalised drug treatments. For instance, for the TCGA-EJ-5527 patient, the use of MYC\_MAX complex inhibitor reduced *Proliferation* to 66%. For this patient, combining MYC\_MAX with other inhibitors, such as AR or AKT, did not further reduce the *Proliferation* score (67% in these cases). Other patients have MYC\_MAX as an interesting drug target, but the inhibition of this complex did not have such a dramatic effect on their *Proliferation* scores as in the case of TCGA-EJ-5527. Likewise, for the TCGA-H9-A6BX patient, the use of SPOP inhibitor increased *Apoptosis* by 87%, while the use of a combination of cFLAR and SPOP inhibitors further increased *Apoptosis* by 89%. For the rest of this section, we focus on the analysis of clinical groups rather than individuals.

Studying the decrease of *Proliferation*, we found that AKT is the top hit in Gleason Grades 1, 2, 3, and 4, seconded by EGFR and SPOP in Grade 1, by SPOP and PIP3 in Grade 2, by PIP3 and AR in Grade 3, and by CyclinD and MYC\_MAX in Grade 4. MYC\_MAX is the top hit in Grade 5, seconded by AR (Appendix 1, Section 4.2, Appendix figure 19). In regards to the increase of *Apoptosis*, SPOP is the top hit in all grades, seconded by SSH in Grades 1, 2 and 3 and by AKT in Grade 4 (Appendix 1, Section 4.2, Appendix figure 20). It is interesting to note here that many of these genes are targeted by drugs (Table 1). Notably, AR is the target of the drug Enzalutamide, which is indicated for men with an advanced stage of the disease (Scott, 2018), or that MYC is the target of BET bromodomain inhibitors and are generally effective in castration-resistant prostate cancer cases (Coleman et al., 2019).

The work on patient data provided some possible insights and suggested patient- and grade-specific potential targets. To validate our approach experimentally, we personalised the prostate model to different prostate cell lines, where we performed drug assays to confirm the predictions of the model.

## Personalised drug predictions of LNCaP Boolean model

We applied the methodology for personalisation of the prostate model to eight prostate cell lines available in GDSC (Iorio et al, 2016): 22RV1, BPH-1, DU-145, NCI-H660, PC-3, PWR-1E and VCaP (results in Appendix File, Section 5 and are publicly available in Supplementary File 5). We decided to focus the validation on one cell line, LNCaP.

LNCaP, first isolated from a human metastatic prostate adenocarcinoma found in a lymph node (Horoszewicz et al, 1983), is one of the most widely used cell lines for prostate cancer studies. Androgen-sensitive LNCaP cells are representative of patients sensitive to treatments as opposed to resistant cell lines such as DU-145. Additionally, LNCaP cells have been used to obtain numerous subsequent derivatives with different characteristics (Cunningham and You, 2015).

The LNCaP personalisation was performed based on mutations as discrete data and RNA-Seq as continuous data. The resulting LNCaP-specific Boolean model was then used to identify all possible combinations of mutations (interpreted as effects of therapies) and to study the synergy of these perturbations. For that purpose, we automatically performed single and double mutant analyses on the LNCaP-specific model (knock-out and overexpression) (Montagud et al., 2017) and focused on the model phenotype probabilities

as read-outs of the simulations. The analysis of the complete set of simulations for the 32258 mutants can be found in the Appendix 1, Section 6.1 and in Supplementary File 6, where the LNCaP-cell-line-specific mutants and their phenotype scores are reported for all mutants. Among all combinations, we identified the top 20 knock-out mutations that depleted *Proliferation* or increased *Apoptosis* the most. As some of them overlapped, we ended up with 29 nodes: *AKT*, *AR*, *ATR*, *AXIN1*, *Bak*, *BIRC5*, *CDH2*, *cFLAR*, *CyclinB*, *CyclinD*, *E2F1*, *eEF2K*, *eEF2*, *eEF2K*, *EGFR*, *ERK*, *HSPs*, *MED12*, *mTORC1*, *mTORC2*, *MYC*, *MYC\_MAX*, *PHDs*, *PI3K*, *PIP3*, *SPOP*, *TAK1*, *TWIST1*, and *VHL*. We used the scores of these nodes to further trim down the list to have 10 final nodes (*AKT*, *AR*, *cFLAR*, *EGFR*, *ERK*, *HSPs*, *MYC\_MAX*, *SPOP* and *PI3K*) and added 7 other nodes whose genes are considered relevant in cancer biology, such as *AR\_ERG* fusion, *Caspase8*, *HIF1*, *GLUT1*, *MEK1\_2*, *p14ARF*, *ROS* and *TERT* (Table 1). We did not consider the overexpression mutants as they have a very difficult translation to drug uses and clinical practices.

To further analyse the mutant effects, we simulated the LNCaP model with increasing node inhibition values to mimic the effect of drugs' dosages using a methodology we specifically developed for these purposes (PROFILE\_v2 and available at [https://github.com/ArnaudMontagud/PROFILE\\_v2](https://github.com/ArnaudMontagud/PROFILE_v2)). Six simulations were done for each inhibited node, with 100% of node activity (no inhibition), 80%, 60%, 40%, 20% and 0% (full knock-out) (see Methods). A nutrient-rich media with EGF was used for these simulations, and we show results on three additional sets of initial conditions in the Appendix 1, Section 6, Appendix figure 27: a nutrient-rich media with androgen, with androgen and EGF, and with none, that correspond to experimental conditions that are tested here. We applied this gradual inhibition, using increasing drugs' concentrations, to a reduced list of drug-targeted genes relevant for cancer progression (Table 1). We confirmed that the inhibition of different nodes affected differently the probabilities of the outputs (Appendix 1, Section 7.3.1, Appendix figures 34 and 35). Notably, the *Apoptosis* score was slightly promoted when knocking out *SPOP* under all growth conditions (Appendix 1, Section 7.3.1, Appendix figure 35). Likewise, *Proliferation* depletion was accomplished when *HSPs* or *MYC\_MAX* were inhibited under all conditions and, less notably, when *ERK*, *EGFR*, *SPOP* or *PI3K* were inhibited (Appendix 1, Section 7.3.1, Appendix figure 35).

Additionally, these gradual inhibition analyses can be combined to study the interaction of two simultaneously inhibiting nodes (Appendix 1, Section 7.3.2, Appendix figure 36 and 37). For instance, the combined gradual inhibition of *ERK* and *MYC\_MAX* nodes affects the *Proliferation* score in a balanced manner (Figure 5A) even though *MYC\_MAX* seems to affect this phenotype more, notably at low activity levels. By extracting subnetworks of interaction around *ERK* and *MYC\_MAX* and comparing them, we found that the pathways they belong to have complementary downstream targets participating in cell proliferation through targets in MAPK and cell cycle pathways. This complementarity could explain the synergistic effects observed (Figure 5A and 5C).

Lastly, drug synergies can be studied using Bliss Independence using the results from single and combined simulations with gradual inhibitions. This score compares the combined effect of two drugs with the effect of each one of them, with a synergy when the value of this score is lower than 1. We found that the combined inhibition of *ERK* and *MYC\_MAX* nodes on the *Proliferation* score was synergistic (Figure 5C). Another synergistic pair is the combined gradual inhibition of *HSPs* and *PI3K* nodes that also affects the *Proliferation* score in a joint manner (Figure 5B), with some Bliss Independence synergy found (Figure 5D). A complete

330 study on the Bliss Independence synergy of all the drugs considered in the present work on  
331 *Proliferation* and *Apoptosis* phenotypes can be found in Appendix 1, Section 7.3.2, Appendix  
332 figures 38 and 39.

### 333 Experimental validation of predicted targets

#### 334 Drugs associated with the proposed targets

335 To identify drugs that could act as potential inhibitors of the genes identified with the Boolean  
336 model, we explored the drug-target associations in DrugBank (Wishart et al., 2018) and  
337 ChEMBL (Gaulton et al., 2017). We found drugs that targeted almost all genes  
338 corresponding to the nodes of interest in Table 1, except for cFLAR, p14ARF and SPOP.  
339 However, we could not identify experimental cases where drugs targeting both members of  
340 the proposed combinations were available (Appendix 1, Section 7.1 and in Supplementary  
341 File 6). One possible explanation is that the combinations predicted by the model suggest, in  
342 some cases, to overexpress the potential target and most of the drugs available act as  
343 inhibitors of their targets.

344 Using the cell-line specific models, we tested if the LNCaP cell line was more sensitive than  
345 the rest of the prostate cell lines to the LNCaP-specific drugs identified in Table 1. We  
346 compared GDSC's Z-score of these drugs in LNCaP with their Z-scores in all GDSC cell  
347 lines (Figure 6 and Appendix 1, Section 7.2, Appendix figure 33). We observed that LNCaP  
348 is more sensitive to drugs targeting AKT or TERT than the rest of the studied prostate cell  
349 lines. Furthermore, we saw that the drugs that targeted the genes included in the model  
350 allowed the identification of cell line specificities (Appendix 1, Section 7.1). For instance,  
351 target enrichment analysis showed that LNCaP cell lines are especially sensitive to drugs  
352 targeting PI3K/AKT/mTOR, hormone-related (AR targeting) and Chromatin (bromodomain  
353 inhibitors, regulating Myc) pathways (adjusted p-values from target enrichment: 0.001, 0.001  
354 and 0.032, respectively, Appendix 1, Section 7.1, Appendix table 2), which corresponds to  
355 the model predictions (Table 1). Also, the LNCaP cell line is more sensitive to drugs  
356 targeting model-identified nodes than to drugs targeting other proteins (Appendix 1, Section  
357 7.1, Appendix figure 32, Mann-Whitney p-value 0.00041), and this effect is specific for  
358 LNCaP cell line (Mann-Whitney p-values ranging from 0.0033 to 0.38 for other prostate  
359 cancer cell lines).

360 Overall, the drugs proposed through this analysis suggest the possibility to repurpose drugs  
361 that are used in treating other forms of cancer for prostate cancer and open the avenue for  
362 further experimental validations based on these suggestions.

#### 363 Experimental validation of drugs in LNCaP

364 To validate the model predictions of the candidate drugs, we selected four drugs that target  
365 HSPs and PI3K and tested them in LNCaP cell line experiments by using endpoint cell  
366 viability measurement assays and real-time cell survival assays using the xCELLigence  
367 system (see Methods). The drug selection was a compromise between the drugs identified  
368 by our analyses (Table 1) and their effect in diminishing LNCaP's proliferation (see the  
369 previous section). In both assays, drugs that target HSP90AA1 and PI3K/AKT pathway  
370 genes retrieved from the model analyses were found to be effective against cell proliferation.

371 The Hsp90 chaperone is expressed abundantly and plays a crucial role in the correct folding  
372 of a wide variety of proteins such as protein kinases and steroid hormone receptors (Schopf  
373 et al., 2017). Hsp90 can act as a protector of less stable proteins produced by DNA  
374 mutations in cancer cells (Barrott and Haystead, 2013; Hessenkemper and Baniahmad,  
375 2013). Currently, Hsp90 inhibitors are in clinical trials for multiple indications in cancer (Chen  
376 et al., 2019; Iwai et al., 2012; Le et al., 2017). The PI3K/AKT signalling pathway controls  
377 many different cellular processes such as cell growth, motility, proliferation, and apoptosis  
378 and is frequently altered in different cancer cells (Carceles-Cordon et al., 2020; Shorning et  
379 al., 2020). Many PI3K/AKT inhibitors are in different stages of clinical development, and  
380 some of them are approved for clinical use (Table 1).

381 Notably, Hsp90 (NMS-E973,17-DMAG) and PI3K/AKT pathway (PI-103, Pictilisib) inhibitors  
382 showed a dose-dependent activity in the endpoint cell viability assay determined by the  
383 fluorescent resazurin after a 48-hour incubation (Figure 7). This dose-dependent activity is  
384 more notable in Hsp90 drugs (NMS-E973,17-DMAG) than in PI3K/AKT pathway (Pictilisib)  
385 ones and very modest for PI-103.

386 We studied the real-time response of LNCaP cell viability upon drug addition and saw that  
387 the LNCaP cell line is sensitive to Hsp90 and PI3K/AKT pathway inhibitors (Figure 8 and 9,  
388 respectively). Both Hsp90 inhibitors tested, 17-DMAG and NMS-E973, reduced the cell  
389 viability 12 hours after drug supplementation (Figure 8A for 17-DMAG and Figure 8B for  
390 NMS-E973), with 17-DMAG having a stronger effect and in a more clear concentration-  
391 dependent manner than NMS-E973 (Appendix 1, Section 8, Appendix figure 40, panels B-D  
392 for 17-DMAG and panels F-H for NMS-E973).

393 Likewise, both PI3K/AKT pathway inhibitors tested, Pictilisib and PI-103, reduced the cell  
394 viability immediately after drug supplementation (Figure 9A for Pictilisib and Figure 9B for PI-  
395 103), in a concentration-dependent manner (Appendix 1, Section 8, Appendix figure 41,  
396 panels B-D for Pictilisib and panels F-H for PI-103). In addition, Hsp90 inhibitors had a more  
397 prolonged effect on the cells' proliferation than PI3K/AKT pathway inhibitors.

## 398 Discussion

399 Clinical assessment of cancers is moving towards more precise, personalised treatments, as  
400 the times of one-size-fits-all treatments are no longer appropriate, and patient-tailored  
401 models could boost the success rate of these treatments in clinical practice. In this study, we  
402 set out to develop a methodology to investigate drug treatments using personalised Boolean  
403 models. Our approach consists of building a model that represents the patient-specific  
404 disease status and retrieving a list of proposed interventions that affect this disease status,  
405 notably by reducing its pro-cancerous behaviours. In this work, we have showcased this  
406 methodology by applying it to TCGA prostate cancer patients and to GDSC prostate cancer  
407 cell lines, finding patient- and cell-line-specific targets and validating selected cell-line-  
408 specific predicted targets (Figure 1).

409 First, a prostate cancer Boolean model that encompasses relevant signalling pathways in  
410 cancer was constructed based on already published models, experimental data analyses  
411 and pathway databases (Figure 2). The influence network and the assignment of logical  
412 rules for each node of this network were obtained from known interactions described in the

413 literature (Figure 3). This model describes the regulation of invasion, migration, cell cycle,  
414 apoptosis, androgen and growth factors signalling in prostate cancer (Appendix File, Section  
415 1).

416 Second, from this generic Boolean model, we constructed personalised models using the  
417 different datasets, i.e. 488 patients from TCGA and eight cell lines from GDSC. We obtained  
418 Gleason-score-specific behaviours for TCGA's patients when studying their *Proliferation* and  
419 *Apoptosis* scores, observing that high *Proliferation* scores are higher in high Gleason grades  
420 (Figure 4). Thus, the use of these personalised models can help rationalise the relationship  
421 of Gleason grading with some of these phenotypes.

422 Likewise, GDSC data was used with the prostate model to obtain prostate-specific cell-line  
423 models (Figure 6). These models show differential behaviours, notably in terms of *Invasion*  
424 and *Proliferation* phenotypes (Appendix 1, Section 5, Appendix figure 21). One of these cell-  
425 line-specific models, LNCaP, was chosen, and the effects of all its genetic perturbations  
426 were thoroughly studied. We studied 32258 mutants, including single and double mutants,  
427 knock-out and over-expressed, and their phenotypes (Appendix 1, Section 6.1, Appendix  
428 figures 28 and 29). 32 knock-out perturbations that depleted *Proliferation* and/or increased  
429 *Apoptosis* were identified, and 16 of them were selected for further analyses (Table 1). The  
430 LNCaP-specific model was simulated using different initial conditions that capture different  
431 growth media's specificities, such as RPMI media with and without androgen or epidermal  
432 growth factor (Appendix 1, Section 6, Appendix figure 27).

433 Third, these personalised models were used to simulate the inhibition of druggable genes  
434 and proteins, uncovering new treatment's combination and their synergies. We developed a  
435 methodology to simulate drug inhibitions in Boolean models, termed PROFILE\_v2, as an  
436 extension of previous works (Béal et al., 2019). The LNCaP-specific model was used to  
437 obtain simulations with nodes and pairs of nodes corresponding to the genes of interest  
438 inhibited with varying strengths. This study allowed us to compile a list of potential targets  
439 (Table 1) and to identify potential synergies among genes in the model (Figure 5). Some of  
440 the drugs that targeted these genes, such as AKT and TERT, were identified in GDSC as  
441 having more sensitivity in LNCaP than in the rest of the prostate cancer cell lines (Figure 6).  
442 In addition, drugs that targeted genes included in the model allowed the identification of cell  
443 line specificities (Appendix 1, Section 5).

444 Fourth, we validated the effect of Hsp90 and PI3K/AKT pathway inhibitors on the LNCaP cell  
445 line experimentally, finding a concentration-dependent inhibition of the cell line viability as  
446 predicted, confirming the role of the drugs targeting these proteins in reducing LNCaP's  
447 proliferation (Figure 7 and 8). Notably, these targets have been studied in other works on  
448 prostate cancer (Chen et al., 2019; Le et al., 2017).

449 The study presented here enables the study of drug combinations and their synergies. One  
450 reason for searching for combinations of drugs is that these have been described for  
451 allowing the use of lower doses of each of the two drugs reducing their toxicity (Bayat  
452 Mokhtari et al., 2017), evading compensatory mechanisms and combating drug resistances  
453 (Al-Lazikani et al., 2012; Krzyszczyk et al., 2018).

454 Even if this approach is attractive and promising, it has some limitations. The scope of  
455 present work is to test this methodology on a prostate model and infer patient-specific

456 prostate cancer treatments. The method need to be adapted if it were to be expanded to  
457 study other cancers by using other models and target lists. The analyses performed with the  
458 mathematical model do not aim to predict drug dosages *per se* but to help in the  
459 identification of potential candidates. The patient-specific changes in *Proliferation* and  
460 *Apoptosis* scores upon mutation are maximal theoretical yields that are used to rank the  
461 different potential treatments and should not be used as a direct target for experimental  
462 results or clinical trials. Our methodology suggests treatments for individual patients, but the  
463 obtained results vary greatly from patient to patient, which is not an uncommon issue of  
464 personalised medicine (Ciccarese et al., 2017; Molinari et al., 2018). This variability is an  
465 economic challenge for labs and companies to pursue true patient-specific treatments and  
466 also poses challenges in clinical trial designs aimed at validating the model based on the  
467 selection of treatments (Cunanan et al., 2017). Nowadays, and because of these constraints,  
468 it might be more commercially interesting to target group-specific treatments, which can be  
469 more easily related to clinical stages of the disease.

470 Mathematical modelling of patient profiles helps to classify them in groups with differential  
471 characteristics, providing, in essence, a grade-specific treatment. We, therefore, based our  
472 analysis on clinical grouping defined by the Gleason grades, but some works have  
473 emphasised the difficulty to properly assess them (Chen and Zhou, 2016) and, as a result,  
474 may not be the perfect predictor for the patient subgrouping in this analysis, even though it is  
475 the only available one for these datasets. The lack of subgrouping that stratifies patients  
476 adequately may undermine the analysis of our results and could explain the *Proliferation* and  
477 *Apoptosis* scores of high-grade and low-grade Gleason patients.

478 Moreover, the behaviours observed in the simulations of the cell-lines-specific models do not  
479 always correspond to what is reported in the literature. The differences between simulation  
480 results and biological characteristics could be addressed in further studies by including other  
481 pathways, for example, better describing the DNA repair mechanisms, or by tailoring the  
482 model with different sets of data, as the data used to personalise these models do not allow  
483 for clustering these cell lines according to their different characteristics (Appendix 1, Section  
484 5, Appendix figure 24 and 25). In this sense, another limitation is that we use static data (or a  
485 snapshot of dynamic data) to build dynamic models and to study its stochastic results. Thus,  
486 these personalised models would likely improve their performance if they were fitted to  
487 dynamic data (Saez-Rodriguez and Blüthgen, 2020) or quantitative versions of the models  
488 were built, such as ODE-based, that may capture more fine differences among cell lines. As  
489 perspectives, we are working on integrating these models in multiscale models to study the  
490 effect of the tumour microenvironment (Ponce-de-Leon et al., 2021, 2022), on including  
491 information to simulate multiple reagents targeting a single node of the model, on scaling  
492 these multiscale models to exascale high-performance computing clusters (Montagud et al.,  
493 2021; Saxena et al., 2021), and on streamlining these studies using workflows in computing  
494 clusters to fasten the processing of new, bigger cohorts, as in the PerMedCoE project  
495 (<https://permedcoe.eu/>).

496 The present work contributes to efforts aimed at using modelling (Eduati et al., 2020; Rivas-  
497 Barragan et al., 2020; Gómez Tejeda Zañudo et al., 2017) and other computational methods  
498 (Madani Tonekaboni et al., 2018; Menden et al., 2019) for the discovery of novel drug  
499 targets and combinatorial strategies. Our study expands the prostate drug catalogue and  
500 improves predictions of the impact of these in clinical strategies for prostate cancer by  
501 proposing and grading the effectiveness of a set of drugs that could be used off-label or

502 repurposed. The insights gained from this study present the potential of using personalised  
503 models to obtain precise, personalised drug treatments for cancer patients.

504 **Materials and Methods**

505 **Data acquisition**

506 Publicly available data of 489 human prostate cancer patients from TCGA described in  
507 (Hoadley et al., 2018) were used in the present work. We gathered mutations, CNA, RNA  
508 and clinical data from cBioPortal  
509 ([https://www.cbiportal.org/study/summary?id=prad\\_tcga\\_pan\\_can\\_atlas\\_2018](https://www.cbiportal.org/study/summary?id=prad_tcga_pan_can_atlas_2018)) for all of  
510 these samples resulting in 488 with complete omics datasets.

511 Publicly available data of cell lines used in the present work were obtained from the  
512 Genomics of Drug Sensitivity in Cancer database (GDSC) (Iorio et al., 2016). Mutations,  
513 CNA and RNA data, as well as cell lines descriptors, were downloaded from  
514 (<https://www.cancerrxgene.org/downloads>). In this work, we have used 3- and 5-stage  
515 Gleason grades. Their correspondence is the following: GG Low is GG 1, GG Intermediate is  
516 GG 2 and 3, and GG High is GG 4 and 5.

517 All these data were used to personalise Boolean models using our PROFILE method (Béal  
518 et al., 2019).

519 **Prior knowledge network construction**

520 Several sources were used in building this prostate Boolean model and, in particular, the  
521 model published by Fumiā and Martins (2013). This model includes several signalling  
522 pathways such as the ones involving receptor tyrosine kinase (RTKs), phosphatidylinositol 3-  
523 kinase (PI3K)/AKT, WNT/b-Catenin, transforming growth factor-b (TGF-b)/Smads, cyclins,  
524 retinoblastoma protein (Rb), hypoxia-inducible transcription factor (HIF-1), p53 and ataxia-  
525 telangiectasia mutated (ATM)/ataxia-telangiectasia and Rad3-related (ATR) protein kinases.  
526 The model includes these pathways as well as the substantial cross-talks among them. For  
527 a complete description of the process of construction, see Appendix 1, Section 1.

528 The model also includes several pathways that have a relevant role in our datasets identified  
529 by ROMA (Martignetti et al., 2016), a software that uses the first principal component of a  
530 PCA analysis to summarise the coexpression of a group of genes in the gene set, identifying  
531 significantly overdispersed pathways with a relevant role in a given set of samples. This  
532 software was applied to the TCGA transcriptomics data using the gene sets described in the  
533 Atlas of Cancer Signaling Networks, ACSN (Kuperstein et al., 2015) ([www.acsn.curie.fr](http://www.acsn.curie.fr)) and  
534 in Hallmarks (Liberzon et al., 2015) (Appendix 1, Section 1.1.3, Appendix figure 1) and  
535 highlighted the signalling pathways that show high variance across all samples, suggesting  
536 candidate pathways and genes. Additionally, OmniPath (Türei et al., 2021) was used to  
537 extend the model and complete it, connecting the nodes from Fumiā and Martins and the  
538 ones from ROMA analysis. OmniPath is a comprehensive collection of literature-curated  
539 human signalling pathways, which includes several databases such as Signor (Perfetto et  
540 al., 2016) or Reactome (Fabregat et al., 2016) and that can be queried using pypath, a  
541 Python module for molecular networks and pathways analyses.

542 Fusion genes are frequently found in human prostate cancer and have been identified as a  
543 specific subtype marker (The Cancer Genome Atlas Research Network, 2015). The most  
544 frequent is **TMPRSS2:ERG**, as it involves the transcription factor ERG, which leads to cell-  
545 cycle progression. ERG fuses with the AR-regulated TMPRSS2 gene promoter to form an  
546 oncogenic fusion gene that is especially common in hormone-refractory prostate cancer,  
547 conferring androgen responsiveness to ERG. A literature search reveals that ERG directly  
548 regulates EZH2, oncogene c-Myc and many other targets in prostate cancer (Kunderfranco  
549 et al., 2010).

550 We modelled the gene fusion with activation of ERG by the decoupling of ERG in a special  
551 node *AR\_ERG* that is only activated by the *AR* when the *fused\_event* input node is active. In  
552 the healthy case, *fused\_event* (that represents TMPRSS2:ERG fusion event) is fixed to 0 or  
553 inactive. The occurrence of the gene fusion is represented with the model perturbation  
554 where *fused\_event* is fixed to 1. This *AR\_ERG* node is further controlled by tumour  
555 suppressor NKX3-1 that accelerates *DNA\_repair* response, and avoids the gene fusion  
556 **TMPRSS2:ERG**. Thus, loss of NKX3-1 favours recruitment to the ERG gene breakpoint of  
557 proteins that promote error-prone non-homologous end-joining (Bowen et al., 2015).

558 The network was further documented using up-to-date literature and was constructed using  
559 GINsim (Chaouiya et al., 2012), which allowed us to study its stable states and network  
560 properties.

## 561 Boolean model construction

562 We converted the network to a Boolean model by defining a regulatory graph, where each  
563 node is associated with discrete levels of activity (0 or 1). Each edge represents a regulatory  
564 interaction between the source and target nodes and is labelled with a threshold and a sign  
565 (positive or negative). The model is completed by logical rules (or functions), which assign a  
566 target value to each node for each regulator level combination (Abou-Jaoudé et al., 2016;  
567 Chaouiya et al., 2012). The regulatory graph was constructed using GINsim software  
568 (Chaouiya et al., 2012) and then exported in a format readable by MaBoSS software (see  
569 below) in order to perform stochastic simulations on the Boolean model.

570 The final model has a total of 133 nodes and 449 edges (Supplementary File 1) and includes  
571 pathways such as androgen receptor and growth factor signalling, several signalling  
572 pathways (**Wnt**, **NFKB**, **PI3K/AKT**, **MAPK**, **mTOR**, **SHH**), cell cycle, epithelial-mesenchymal  
573 transition (**EMT**), Apoptosis, DNA damage, etc. This model has 9 inputs (*EGF*, *FGF*, *TGF  
beta*, *Nutrients*, *Hypoxia*, *Acidosis*, *Androgen*, *TNF alpha* and *Carcinogen presence*) and 6  
575 outputs (*Proliferation*, *Apoptosis*, *Invasion*, *Migration*, (bone) *Metastasis* and *DNA repair*).  
576 Note that a node in the network can represent complexes or families of proteins (e.g., **AMPK**  
577 represents the genes **PRKAA1**, **PRKAA2**, **PRKAB1**, **PRKAB2**, **PRKAG1**, **PRKAG2**,  
578 **PRKAG3**). The correspondence can be found in “Montagud2021\_interactions\_sources.xlsx”  
579 and “Montagud2021\_nodes\_in\_pathways.xlsx” in Supplementary File 1.

580 This model was deposited in the GINsim Database with identifier 252  
581 (<http://ginsim.org/model/signalling-prostate-cancer>) and in BioModels (Malik-Sheriff et al.,  
582 2019) with identifier **MODEL2106070001** (<https://www.ebi.ac.uk/biomodels/MODEL2106070001>). Supplementary File 1 is provided as

584 a zipped folder with the model in several formats: MaBoSS, GINsim, SBML, as well as  
585 images of the networks and their annotations. An extensive description of the model  
586 construction can be found in the Appendix 1, Section 1.

## 587 Stochastic Boolean model simulation

588 MaBoSS (Stoll et al., 2017, 2012) is a C++ software for stochastically simulating  
589 continuous/discrete-time Markov processes defined on the state transition graph (STG)  
590 describing the dynamics of a Boolean model (for more details, see (Abou-Jaoudé et al.,  
591 2016; Chaouiya et al., 2012)). MaBoSS associates transition rates to each node's activation  
592 and inhibition, enabling it to account for different time scales of the processes described by  
593 the model. Probabilities to reach a phenotype (to have value ON) are thus computed by  
594 simulating random walks on the probabilistic STG. Since a state in the STG can combine the  
595 activation of several phenotypic variables, not all phenotype probabilities are mutually  
596 exclusive (like the ones in Appendix 1, Section 6.1, Appendix figure 28). Using MaBoSS, we  
597 can study an increase or decrease of a phenotype probability when the model variables are  
598 altered (nodes status, initial conditions and transition rates), which may correspond to the  
599 effect of particular genetic or environmental perturbation. In the present work, the outputs of  
600 MaBoSS focused on the readouts of the model, but this can be done for any node of a  
601 model.

602 MaBoSS applies Monte-Carlo kinetic algorithm (i.e. Gillespie algorithm) to the STG to  
603 produce time trajectories (Stoll et al., 2017, 2012), so time evolution of probabilities are  
604 estimated once a set of initial conditions are defined and a maximum time is set to ensure  
605 that the simulations reach asymptotic solutions. Results are analysed in two ways: (1) the  
606 trajectories for particular model states (states of nodes) can be interpreted as the evolution  
607 of a cell population as a function of time, and (2) asymptotic solutions can be represented as  
608 pie charts to illustrate the proportions of cells in particular model states. Stochastic  
609 simulations with MaBoSS have already been successfully applied to study several Boolean  
610 models (Calzone et al., 2010; Cohen et al., 2015; Remy et al., 2015). A description of the  
611 methods we have used for the simulation of the model can be found in the Appendix 1,  
612 Section 2.

## 613 Data tailoring the Boolean model

614 Logical models were tailored to a dataset using PROFILE to obtain personalised models that  
615 capture the particularities of a set of patients (Béal et al., 2019) and cell lines (Béal et al.,  
616 2021). Proteomics, transcriptomics, mutations and CNA data can be used to modify different  
617 variables of the MaBoSS framework, such as node activity status, transition rates and initial  
618 conditions. The resulting ensemble of models is a set of personalised variants of the original  
619 model that can show great phenotypic differences. Different recipes (use of a given data  
620 type to modify a given MaBoSS variable) can be tested to find the combination that better  
621 correlates to a given clinical or otherwise descriptive data.

622 In the present case, TCGA-patient-specific models were built using mutations, CNA and/or  
623 RNA expression data. After studying the effect of these recipes in the clustering of patients

according to their Gleason grouping (Appendix 1, Section 4.1, Appendix figure 10-14), we chose to use mutations and CNA as discrete data and RNA expression as continuous data.

Likewise, we tried different personalisation recipes to personalise the GDSC prostate cell lines models, but as they had no associated clinical grouping features, we were left with the comparison of the different values for the model's outputs among the recipes (Appendix 1, Section 5, Appendix figure 23). We used mutation data as discrete data and RNA expression as continuous data as it included the most quantity of data and reproduced the desired results (Appendix 1, Section 5, Appendix figure 23). We decided not to include CNA as discrete data as it forced LNCAP proliferation to be zero by forcing the E2F1 node to be 0 and the SMAD node to be 1 throughout the simulation (for more details, refer to Appendix 1, Section 5).

More on PROFILE's methodology can be found in its own work (Béal et al., 2019) and at its dedicated GitHub repository: <https://github.com/sysbio-curie/PROFILE>. A description of the methods we have used for the personalisation of the models can be found in the Appendix 1, Section 3. The analysis of the TCGA personalisations and their patient-specific drug treatments can be found in Appendix 1, Section 4. The analysis of the prostate cell lines personalisations can be found in Appendix 1, Section 5, with a special focus on the LNCaP cell line model analysis in Section 6.

## High-throughput mutant analysis of Boolean models

MaBoSS allows the study of knock-out or loss-of-function (node forced to 0) and gain-of-function (node forced to 1) mutants as genetic perturbations and of initial conditions as environmental perturbations. Phenotypes' stabilities against perturbations can be studied and allow to determine driver mutations that promote phenotypic transitions (Montagud et al., 2017).

Genetic interactions were thoroughly studied using our pipeline of computational methods for Boolean modelling of biological networks (available at [https://github.com/sysbio-curie/Logical\\_modelling\\_pipeline](https://github.com/sysbio-curie/Logical_modelling_pipeline)). LNCaP-specific Boolean model was used to perform single and double knock-out (node forced to 0) and gain-of-function (node forced to 1) mutants for each one of the 133 nodes, resulting in a total of 32258 models. These were simulated under the same initial conditions, their phenotypic results were collected, and a PCA was applied on the wild-type-centred matrix (Appendix 1, Section 6.1, Appendix figure 28 and 29). In addition, we found that the LNCaP model is very robust against perturbations of its logical rules by systematically changing an AND for an OR gate or vice versa in all of its logical rules (Appendix 1, Section 6.2, Appendix figure 30 and 31).

The 488 TCGA-patient-specific models were studied in a similar way, but only perturbing 16 nodes shortlisted for their therapeutic target potential (AKT, AR, Caspase8, cFLAR, EGFR, ERK, GLUT1, HIF-1, HSPs, MEK1\_2, MYC\_MAX, p14ARF, PI3K, ROS, SPOP and TERT). Then, the nodes that mostly contributed to a decrease of *Proliferation* (Appendix 1, Section 4.2, Appendix figure 19) or an increase in *Apoptosis* (Appendix 1, Section 4.2, Appendix figure 20) were gathered from the 488 models perturbed.

Additionally, the results of the LNCaP model's double mutants were used to quantify the level of genetic interactions (epistasis or otherwise (Drees et al., 2005)) between two model

666 genetic perturbations (resulting from either the gain-of-function mutation of a gene or from its  
667 knock-out or loss-of-function mutation) with respect to wild type phenotypes' probabilities  
668 (Calzone et al., 2015). The method was applied to the LNCaP model studying *Proliferation*  
669 and *Apoptosis* scores (Appendix 1, Section 7.3.2, Appendix figure 34 and 35).

670 This genetic interaction study uses the following equation for each gene pair, which is  
671 equation 2 in Calzone et al, (2015):

672  $\epsilon_\phi(A, B) = f_\phi^{AB} - \psi(f_\phi^A, f_\phi^B)$  (1)

673 Where  $f_\phi^A$  and  $f_\phi^B$  are phenotype  $\phi$  fitness values of single gene defects,  $f_\phi^{AB}$  is the  
674 phenotype  $\phi$  fitness of the double mutant, and  $\psi(x, y)$  is one of the four functions:

675  $\psi^{ADD}(x, y) = x + y$  (additive)

676  $\psi^{LOG}(x, y) = \log_2((2^x - 1)(2^y - 1) + 1)$  (log)

677  $\psi^{MLT}(x, y) = x * y$  (multiplicative)

678  $\psi^{MIN}(x, y) = \min(x, y)$  (min) (2)

679 To choose the best definition of  $\psi(x, y)$ , the Pearson correlation coefficient is computed  
680 between the fitness values observed in all double mutants and estimated by the null model  
681 (more information on (Drees et al., 2005)). Regarding  $f_\phi^X$  fitness value, to a given phenotype  
682  $\phi$ ,  $f_\phi^X < 1$  represents deleterious,  $f_\phi^X > 1$  beneficial and  $f_\phi^X \approx 1$  neutral mutation.

## 683 Drug simulations in Boolean models

684 Logical models can be used to simulate the effect of therapeutic interventions and predict  
685 the expected efficacy of candidate drugs on different genetic and environmental  
686 backgrounds by using our PROFILE\_v2 methodology. MaBoSS can perform simulations  
687 changing the proportion of activated and inhibited status of a given node. This can be  
688 determined in the configuration file of each model (see, for instance, the "istate" section of  
689 the CFG files in the Supplementary File 1, 3 and 5). For instance, out of 5000 trajectories of  
690 the Gillespie algorithm, MaBoSS can simulate 70% of them with an activated AKT and 30%  
691 with an inhibited AKT node. The phenotypes' probabilities for the 5000 trajectories are  
692 averaged, and these are considered to be representative of a model with a drug that inhibits  
693 30% of the activity of AKT. The same applies for a combined drug inhibition: a simulation of  
694 50% AKT activity and 50% PI3K will have 50% of them with an activated AKT and 50% with  
695 an activated PI3K. Combining them, this will lead to 25% of the trajectories with both AKT  
696 and PI3K active, 25% with both nodes inactive, 25% with AKT active and 25% with PI3K  
697 active.

698 In the present work, the LNCaP model has been simulated with different levels of node  
699 activity, with 100% of node activity (no inhibition), 80%, 60%, 40%, 20% and 0% (proper  
700 knock-out), under four different initial conditions, a nutrient-rich media that simulates RPMI  
701 Gibco® media with DHT (androgen), with EGF, with both and with none. In terms of the  
702 model, the initial conditions are *Nutrients* is ON and *Acidosis*, *Hypoxia*, *TGF beta*,

703 *Carcinogen* and *TNF alpha* are set to OFF. *EGF* and *Androgen* values vary upon  
704 simulations. We simulated the inhibition of 17 nodes of interest. These were the 16 nodes  
705 from Table 1 with the addition of the fused AR-ERG (Appendix 1, Section 7.3.1, Appendix  
706 figures 34 and 35) and their 136 pairwise combinations (Appendix 1, Section 7.3.2, Appendix  
707 figures 36 and 37). As we used 6 different levels of activity for each node, the resulting  
708 Appendix figures 36 and 37 comprise a total of 4998 simulations for each phenotype (136 x  
709 6 x 6 + 17 x 6).

710 Drug synergies have been studied using Bliss Independence. The Combination Index was  
711 calculated with the following equation (Foucquier and Guedj, 2015):

$$CI = (E_a + E_b - E_a * E_b) / E_{ab} \quad (3)$$

712 Where  $E_a$  and  $E_b$  is the efficiency of the single drug inhibitions and  $E_{ab}$  is the inhibition  
713 resulting from the double drug simulations. A Combination Index ( $CI$ ) below 1 represents  
714 synergy among drugs (Appendix 1, Section 7.3.2, Appendix figures 36 and 37).

715 This methodology can be found in its own repository:  
716 [https://github.com/ArnaudMontagud/PROFILE\\_v2](https://github.com/ArnaudMontagud/PROFILE_v2)

## 718 Identification of drugs associated with proposed targets

719 To identify drugs that could act as potential inhibitors of the genes identified with our models  
720 (Table 1), we explored the drug-target associations in DrugBank (Wishart et al., 2018). For  
721 those genes with multiple drug-target links, only those drugs that are selective and known to  
722 have relevance in various forms of cancer are considered here.

723 In addition to DrugBank searches, we also conducted exhaustive searches in ChEMBL  
724 (Gaulton et al., 2017) (<http://doi.org/10.6019/CHEMBL.database.23>) to suggest potential  
725 candidates for genes whose information is not well documented in Drug Bank. From the  
726 large number of bioactivities extracted from ChEMBL, we filtered human data and  
727 considered only those compounds whose bioactivities fall within a specific threshold  
728 (IC50/Kd/ Ki<100 nM).

729 We performed a target set enrichment analysis using the fgsea method (Korotkevich et al.,  
730 2016) from the piano R package (Väremo et al., 2013). We targeted pathway information  
731 from the GDSC1 and GDSC2 studies (Iorio et al., 2016) as target sets and performed the  
732 enrichment analysis on the normalised drug sensitivity profile of the LNCaP cell line. We  
733 normalised drug sensitivity across cell lines in the following way: cells were ranked from  
734 most sensitive to least sensitive (using ln(IC50) as drug sensitivity metrics), and the rank  
735 was divided by the number of cell lines tested with the given drug. Thus, the most sensitive  
736 cell line has 0, while the most resistant cell line has 1 normalised sensitivity. This rank-based  
737 metric made it possible to analyse all drug sensitivities for a given cell line without drug-  
738 specific confounding factors, like mean IC50 of a given drug, etc. (Appendix 1, Section 7.1  
739 and 7.2).

## 740 Cell culture method

741 For the in vitro drug perturbation validations, we used the androgen-sensitive prostate  
742 adenocarcinoma cell line LNCaP purchased from American Type Culture Collection (ATCC,

743 Manassas, WV, USA). ATCC found no *Mycoplasma* contamination and the cell line was  
744 identified using STR profiling. Cells were maintained in RPMI-1640 culture media (Gibco,  
745 Thermo Fisher Scientific, Waltham, MA, USA) containing 4.5 g/L glucose, 10% foetal bovine  
746 serum (FBS, Gibco), 1X GlutaMAX (Gibco), 1% PenStrep antibiotics (Penicillin G sodium  
747 salt, and Streptomycin sulfate salt, Sigma-Aldrich, St. Louis, MI, USA). Cells were  
748 maintained in a humidified incubator at 37 °C with 5% CO<sub>2</sub> (Sanyo, Osaka, Japan).

## 749 Drugs used in the cell culture experiments

750 We tested two drugs targeted at Hsp90 and two targeted at PI3K complex. 17-DMAG is an  
751 Hsp90 inhibitor with an IC<sub>50</sub> of 62 nM in a cell-free assay (Pacey et al., 2011). NMS-E973 is  
752 an Hsp90 inhibitor with DC<sub>50</sub> of <10 nM for Hsp90 binding (Fogliatto et al., 2013). Pictilisib is  
753 an inhibitor of PI3K $\alpha/\delta$  with IC<sub>50</sub> of 3.3 nM in cell-free assays (Zhan et al., 2017). PI-103 is a  
754 multi-targeted PI3K inhibitor for p110 $\alpha/\beta/\delta/\gamma$  with IC<sub>50</sub> of 2 to 3 nM in cell-free assays and  
755 less potent inhibitor to mTOR/DNA-PK with IC<sub>50</sub> of 30 nM (Raynaud et al., 2009). All drugs  
756 were obtained from commercial vendors and added to the growth media to have  
757 concentrations of 2, 8, 32, 128 and 512 nM for NMS-E973 and 1, 5, 25, 125 and 625 nM for  
758 the rest of the drugs in the endpoint cell viability and of 3.3, 10, 30 uM for all the drugs in the  
759 RT-CES cytotoxicity assay.

## 760 Endpoint cell viability measurements

761 In vitro toxicity of the selected inhibitors was determined using the viability of LNCaP cells,  
762 determined by the fluorescent resazurin (Sigma-Aldrich, Germany) assay as described  
763 previously (Szebeni et al., 2017). Briefly, the LNCaP cells (10000) were seeded into 96-well  
764 plates (Corning Life Sciences, Tewksbury, MA, USA) in 100  $\mu$ l RPMI media and incubated  
765 overnight. Test compounds were dissolved in dimethyl sulfoxide (DMSO, Sigma-Aldrich,  
766 Germany), and cells were treated with an increasing concentration of test compounds: 2, 8,  
767 32, 128 and 512 nM for NMS-E973 and 1, 5, 25, 125 and 625 nM for the rest of the drugs.  
768 The highest applied DMSO content of the treated cells was 0.4%. Cell viability was  
769 determined after 48 hours of incubation. Resazurin reagent (Sigma-Aldrich, Budapest,  
770 Hungary) was added at a final concentration of 25  $\mu$ g/mL. After 2 hours at 37°C 5%, CO<sub>2</sub>  
771 (Sanyo) fluorescence (530 nm excitation/580 nm emission) was recorded on a multimode  
772 microplate reader (Cytofluor4000, PerSeptive Biosystems, Framingham, MA, USA). Viability  
773 was calculated with relation to blank wells containing media without cells and to wells with  
774 untreated cells. Each treatment was repeated in 2 wells per plate during the experiments,  
775 except for the PI-103 treatment with 1 nM in which only one well was used.

776 In these assays, a deviation of 10-15% for in vitro cellular assays is an acceptable variation  
777 as it is a fluorescent assay that detects the cellular metabolic activity of living cells. Thus, in  
778 our analyses, we consider changes above 1.00 to be the same value as the controls.

## 779 Real-time cell electronic sensing (RT-CES) cytotoxicity assay

780 A real-time cytotoxicity assay was performed as previously described (Ozsvári et al., 2010).  
781 Briefly, RT-CES 96-well E-plate (BioTech Hungary, Budapest, Hungary) was coated with  
782 gelatin solution (0.2% in PBS, phosphate buffer saline) for 20 min at 37 °C; then gelatin was

783 washed twice with PBS solution. Growth media (50 µL) was then gently dispensed into each  
784 well of the 96-well E-plate for background readings by the RT-CES system prior to the  
785 addition of 50 µL of the cell suspension containing  $2 \times 10^4$  LNCaP cells. Plates were kept at  
786 room temperature in a tissue culture hood for 30 min prior to insertion into the RT-CES  
787 device in the incubator to allow cells to settle. Cell growth was monitored overnight by  
788 measurements of electrical impedance every 15 min. The next day cells were co-treated with  
789 different drugs with concentrations of 3.3, 10 and 30 µM. Treated and control wells were  
790 dynamically monitored over 72 h by measurements of electrical impedance every 5 min.  
791 Each treatment was repeated in 2 wells per plate during the experiments, except for the 3.3  
792 µM ones in which only one well was used. Continuous recording of impedance in cells was  
793 used as a measurement of the cell growth rate and reflected by the Cell Index value (Solly et  
794 al., 2004).

795 Note that around hour 15, our RT-CES reader had a technical problem caused by a short  
796 blackout in our laboratory and the reader detected a minor voltage fluctuation while the  
797 uninterruptible power supply (UPS) was switched on. This caused differences that are  
798 consistent across all samples and replicates: all wild type and drug reads decrease at that  
799 time point, except Pictilisib that slightly increases. For the sake of transparency and as the  
800 overall dynamic was not affected, we decided to not remove these readings.

801 **Acknowledgements**

802 The authors acknowledge the help provided by Jelena Čuklina at ETH Zurich, Vincent Noël  
803 at Institut Curie, Annika Meert at Barcelona Supercomputing Center and Aurélien Naldi at  
804 INRIA Saclay. XXX thank reviewers

805 The authors acknowledge the technical expertise and assistance provided by the Spanish  
806 Supercomputing Network (Red Española de Supercomputación), as well as the computer  
807 resources used: the LaPalma Supercomputer, located at the Instituto de Astrofísica de  
808 Canarias and MareNostrum4, located at the Barcelona Supercomputing Center.

809 This work has been partially supported by the European Commission under the PrECISE  
810 project ([H2020-PHC-668858](#)), the INFORE project ([H2020-ICT-825070](#)) and the  
811 PerMedCoE ([H2020-ICT-951773](#)).

812

813      **References**

- 814  
815 Abou-Jaoudé W, Chaves M, Gouzé J-L. 2011. A Theoretical Exploration of Birhythmicity in  
816      the p53-Mdm2 Network. *PLoS ONE* **6**:e17075. doi:10.1371/journal.pone.0017075  
817 Abou-Jaoudé W, Traynard P, Monteiro PT, Saez-Rodriguez J, Helikar T, Thieffry D,  
818      Chaouiya C. 2016. Logical Modeling and Dynamical Analysis of Cellular Networks.  
819      *Front Genet* **7**:94. doi:10.3389/fgene.2016.00094  
820 Adamo P, Ladomery MR. 2016. The oncogene ERG: a key factor in prostate cancer.  
821      *Oncogene* **35**:403–414. doi:10.1038/onc.2015.109  
822 Al-Lazikani B, Banerji U, Workman P. 2012. Combinatorial drug therapy for cancer in the  
823      post-genomic era. *Nat Biotechnol* **30**:679–692. doi:10.1038/nbt.2284  
824 Altieri DC, Languino LR, Lian JB, Stein JL, Leav I, van Wijnen AJ, Jiang Z, Stein GS. 2009.  
825      Prostate cancer regulatory networks. *J Cell Biochem* **107**:845–852.  
826      doi:10.1002/jcb.22162  
827 Babtie AC, Stumpf MP. 2017. How to deal with parameters for whole-cell modelling. *J R Soc  
828      Interface* **14**:20170237.  
829 Barrott JJ, Haystead TAJ. 2013. Hsp90, an unlikely ally in the war on cancer. *FEBS J*  
830      **280**:1381–1396. doi:10.1111/febs.12147  
831 Bayat Mokhtari R, Homayouni TS, Baluch N, Morgatskaya E, Kumar S, Das B, Yeger H.  
832      2017. Combination therapy in combating cancer. *Oncotarget* **8**:38022–38043.  
833      doi:10.18632/oncotarget.16723  
834 Béal J, Montagud A, Traynard P, Barillot E, Calzone L. 2019. Personalization of logical  
835      models with multi-omics data allows clinical stratification of patients. *Front Physiol*  
836      **9**:1965. doi:10.3389/fphys.2018.01965  
837 Béal J, Pantolini L, Noël V, Barillot E, Calzone L. 2021. Personalized logical models to  
838      investigate cancer response to BRAF treatments in melanomas and colorectal  
839      cancers. *PLoS Comput Biol* **17**:e1007900. doi:10.1371/journal.pcbi.1007900  
840 Bowen C, Zheng T, Gelmann EP. 2015. NKX3.1 Suppresses TMPRSS2-ERG Gene  
841      Rearrangement and Mediates Repair of Androgen Receptor-Induced DNA Damage.  
842      *Cancer Res* **75**:2686–2698. doi:10.1158/0008-5472.CAN-14-3387  
843 Calzone L, Barillot E, Zinovyev A. 2015. Predicting genetic interactions from Boolean models  
844      of biological networks. *Integr Biol* **7**:921–929. doi:10.1039/C5IB00029G  
845 Calzone L, Tournier L, Fourquet S, Thieffry D, Zhivotovsky B, Barillot E, Zinovyev A. 2010.  
846      Mathematical modelling of cell-fate decision in response to death receptor  
847      engagement. *PLoS Comput Biol* **6**:e1000702. doi:10.1371/journal.pcbi.1000702  
848 Carceles-Cordon M, Kelly WK, Gomella L, Knudsen KE, Rodriguez-Bravo V, Domingo-  
849      Domenech J. 2020. Cellular rewiring in lethal prostate cancer: the architect of drug  
850      resistance. *Nat Rev Urol* **17**:292–307. doi:10.1038/s41585-020-0298-8  
851 Castoria G, D'Amato L, Ciociola A, Giovannelli P, Giraldi T, Sepe L, Paolella G, Barone MV,  
852      Migliaccio A, Auricchio F. 2011. Androgen-induced cell migration: role of androgen  
853      receptor/filamin A association. *PloS One* **6**:e17218.  
854      doi:10.1371/journal.pone.0017218  
855 Chaouiya C, Naldi A, Thieffry D. 2012. Logical Modelling of Gene Regulatory Networks with  
856      GINsim In: Helden J van, Toussaint A, Thieffry D, editors. *Bacterial Molecular  
857      Networks, Methods in Molecular Biology*. Springer New York. pp. 463–479.  
858 Chen N, Zhou Q. 2016. The evolving Gleason grading system. *Chin J Cancer Res* **28**:58–64.  
859      doi:10.3978/j.issn.1000-9604.2016.02.04  
860 Chen W, Li G, Peng J, Dai W, Su Q, He Y. 2019. Transcriptomic analysis reveals that heat  
861      shock protein 90α is a potential diagnostic and prognostic biomarker for cancer. *Eur J  
862      Cancer Prev Off J Eur Cancer Prev Organ ECP*.  
863      doi:10.1097/CEJ.0000000000000549

- 864 Cho S-H, Park S-M, Lee H-S, Lee H-Y, Cho K-H. 2016. Attractor landscape analysis of  
865 colorectal tumorigenesis and its reversion. *BMC Syst Biol* **10**:96.  
866 doi:10.1186/s12918-016-0341-9
- 867 Ciccarese C, Massari F, Iacovelli R, Fiorentino M, Montironi R, Di Nunno V, Giunchi F,  
868 Brunelli M, Tortora G. 2017. Prostate cancer heterogeneity: Discovering novel  
869 molecular targets for therapy. *Cancer Treat Rev* **54**:68–73.  
870 doi:10.1016/j.ctrv.2017.02.001
- 871 Cohen DPA, Martignetti L, Robine S, Barillot E, Zinovyev A, Calzone L. 2015. Mathematical  
872 Modelling of Molecular Pathways Enabling Tumour Cell Invasion and Migration.  
873 *PLoS Comput Biol* **11**:e1004571. doi:10.1371/journal.pcbi.1004571
- 874 Coleman DJ, Gao L, King CJ, Schwartzman J, Urrutia J, Sehrawat A, Tayou J, Balter A,  
875 Burchard J, Chiotti KE, Derrick DS, Sun D, Xia Z, Heiser LM, Alumkal JJ. 2019. BET  
876 bromodomain inhibition blocks the function of a critical AR-independent master  
877 regulator network in lethal prostate cancer. *Oncogene* **38**:5658–5669.  
878 doi:10.1038/s41388-019-0815-5
- 879 Cunanan KM, Iasonos A, Shen R, Begg CB, Gönen M. 2017. An efficient basket trial design.  
880 *Stat Med*. doi:10.1002/sim.7227
- 881 Cunningham D, You Z. 2015. In vitro and in vivo model systems used in prostate cancer  
882 research. *J Biol Methods* **2**. doi:10.14440/jbm.2015.63
- 883 Daroqui MC, Vazquez P, Bal de Kier Joffé E, Bakin AV, Puricelli LI. 2012. TGF- $\beta$  autocrine  
884 pathway and MAPK signaling promote cell invasiveness and in vivo mammary  
885 adenocarcinoma tumor progression. *Oncol Rep* **28**:567–575.  
886 doi:10.3892/or.2012.1813
- 887 Datta D, Aftabuddin M, Gupta DK, Raha S, Sen P. 2016. Human Prostate Cancer Hallmarks  
888 Map. *Sci Rep* **6**:30691. doi:10.1038/srep30691
- 889 De Wever O, Westbroek W, Verloes A, Bloemen N, Bracke M, Gespach C, Bruyneel E,  
890 Mareel M. 2004. Critical role of N-cadherin in myofibroblast invasion and migration in  
891 vitro stimulated by colon-cancer-cell-derived TGF-beta or wounding. *J Cell Sci*  
892 **117**:4691–4703. doi:10.1242/jcs.01322
- 893 Dorier J, Crespo I, Niknejad A, Liechti R, Ebeling M, Xenarios I. 2016. Boolean regulatory  
894 network reconstruction using literature based knowledge with a genetic algorithm  
895 optimization method. *BMC Bioinformatics* **17**:410. doi:10.1186/s12859-016-1287-z
- 896 Drees BL, Thorsson V, Carter GW, Rives AW, Raymond MZ, Avila-Campillo I, Shannon P,  
897 Galitski T. 2005. Derivation of genetic interaction networks from quantitative  
898 phenotype data. *Genome Biol* **6**:R38. doi:10.1186/gb-2005-6-4-r38
- 899 Eduati F, Jaaks P, Wappler J, Cramer T, Merten CA, Garnett MJ, Saez-Rodriguez J. 2020.  
900 Patient-specific logic models of signaling pathways from screenings on cancer  
901 biopsies to prioritize personalized combination therapies. *Mol Syst Biol* **16**:e8664.  
902 doi:10.1525/msb.20188664
- 903 Fabregat A, Sidiropoulos K, Garapati P, Gillespie M, Hausmann K, Haw R, Jassal B, Jupe S,  
904 Korninger F, McKay S, Matthews L, May B, Milacic M, Rothfels K, Shamovsky V,  
905 Webber M, Weiser J, Williams M, Wu G, Stein L, Hermjakob H, D'Eustachio P. 2016.  
906 The Reactome pathway Knowledgebase. *Nucleic Acids Res* **44**:D481–D487.  
907 doi:10.1093/nar/gkv1351
- 908 Faure A, Naldi A, Chaouiya C, Thieffry D. 2006. Dynamical analysis of a generic Boolean  
909 model for the control of the mammalian cell cycle. *Bioinformatics* **22**:e124–e131.  
910 doi:10.1093/bioinformatics/btl210
- 911 Flobak Å, Baudot A, Remy E, Thommesen L, Thieffry D, Kuiper M, Lægreid A. 2015.  
912 Discovery of Drug Synergies in Gastric Cancer Cells Predicted by Logical Modeling.  
913 *PLOS Comput Biol* **11**:e1004426. doi:10.1371/journal.pcbi.1004426
- 914 Fogliatto G, Gianellini L, Brasca MG, Casale E, Ballinari D, Ciomei M, Degrassi A, De Ponti  
915 A, Germani M, Guanci M, Paolucci M, Polucci P, Russo M, Sola F, Valsasina B,  
916 Visco C, Zuccotto F, Donati D, Felder E, Pesenti E, Galvani A, Mantegani S, Isacchi  
917 A. 2013. NMS-E973, a novel synthetic inhibitor of Hsp90 with activity against multiple  
918 models of drug resistance to targeted agents, including intracranial metastases. *Clin*

- 919                   *Cancer Res Off J Am Assoc Cancer Res* **19**:3520–3532. doi:10.1158/1078-  
920                   0432.CCR-12-3512
- 921                  Foucquier J, Guedj M. 2015. Analysis of drug combinations: current methodological  
922                   landscape. *Pharmacol Res Perspect* **3**. doi:10.1002/prp2.149
- 923                  Francis JC, Thomsen MK, Taketo MM, Swain A. 2013.  $\beta$ -catenin is required for prostate  
924                   development and cooperates with Pten loss to drive invasive carcinoma. *PLoS Genet*  
925                   **9**:e1003180. doi:10.1371/journal.pgen.1003180
- 926                  Fumiã HF, Martins ML. 2013. Boolean Network Model for Cancer Pathways: Predicting  
927                   Carcinogenesis and Targeted Therapy Outcomes. *PLoS ONE* **8**:e69008.  
928                   doi:10.1371/journal.pone.0069008
- 929                  Gaulton A, Hersey A, Nowotka M, Bento AP, Chambers J, Mendez D, Mutowo P, Atkinson  
930                   F, Bellis LJ, Cibrián-Uhalte E, Davies M, Dedman N, Karlsson A, Magariños MP,  
931                   Overington JP, Papadatos G, Smit I, Leach AR. 2017. The ChEMBL database in  
932                   2017. *Nucleic Acids Res* **45**:D945–D954. doi:10.1093/nar/gkw1074
- 933                  Gillespie DT. 1976. A general method for numerically simulating the stochastic time  
934                   evolution of coupled chemical reactions. *J Comput Phys* **22**:403–434.  
935                   doi:10.1016/0021-9991(76)90041-3
- 936                  Gleason DF. 1992. Histologic grading of prostate cancer: A perspective. *Hum Pathol*, The  
937                   Pathobiology of Prostate Cancer-Part 1 **23**:273–279. doi:10.1016/0046-  
938                   8177(92)90108-F
- 939                  Gleason DF. 1977. The Veteran's Administration Cooperative Urologic Research Group:  
940                   histologic grading and clinical staging of prostatic carcinomaUrologic Pathology: The  
941                   Prostate. Philadelphia: Lea & Febiger. pp. 171–198.
- 942                  Goldbeter A. 2002. Computational approaches to cellular rhythms. *Nature* **420**:238–245.  
943                   doi:10.1038/nature01259
- 944                  Gómez Tejeda Zañudo J, Scaltriti M, Albert R. 2017. A network modeling approach to  
945                   elucidate drug resistance mechanisms and predict combinatorial drug treatments in  
946                   breast cancer. *Cancer Converg* **1**:5. doi:10.1186/s41236-017-0007-6
- 947                  Grieco L, Calzone L, Bernard-Pierrot I, Radvanyi F, Kahn-Perlès B, Thieffry D. 2013.  
948                   Integrative modelling of the influence of MAPK network on cancer cell fate decision.  
949                   *PLoS Comput Biol* **9**:e1003286. doi:10.1371/journal.pcbi.1003286
- 950                  Hayward SW, Dahiya R, Cunha GR, Bartek J, Deshpande N, Narayan P. 1995.  
951                   Establishment and characterization of an immortalized but non-transformed human  
952                   prostate epithelial cell line: BPH-1. *In Vitro Cell Dev Biol Anim* **31**:14–24.  
953                   doi:10.1007/BF02631333
- 954                  Helikar T, Konvalina J, Heidel J, Rogers JA. 2008. Emergent decision-making in biological  
955                   signal transduction networks. *Proc Natl Acad Sci U S A* **105**:1913–1918.  
956                   doi:10.1073/pnas.0705088105
- 957                  Hessenkemper W, Baniahmad A. 2013. Targeting Heat Shock Proteins in Prostate Cancer.  
958                   *Curr Med Chem* **20**:2731–2740. doi:10.2174/0929867311320220001
- 959                  Hoadley KA, Yau C, Hinoue T, Wolf DM, Lazar AJ, Drill E, Shen R, Taylor AM, Cherniack  
960                   AD, Thorsson Vésteinn, Akbani R, Bowlby R, Wong CK, Wiznerowicz M, Sanchez-  
961                   Vega F, Robertson AG, Schneider BG, Lawrence MS, Noushmehr H, Malta TM,  
962                   Caesar-Johnson SJ, Demchok JA, Felau I, Kasapi M, Ferguson ML, Hutter CM, Sofia  
963                   HJ, Tarnuzzer R, Wang Z, Yang L, Zenklusen JC, Zhang J (Julia), Chudamani S, Liu  
964                   J, Lolla L, Naresh R, Pihl T, Sun Q, Wan Y, Wu Y, Cho J, DeFreitas T, Frazer S,  
965                   Gehlenborg N, Getz G, Heiman DI, Kim J, Lawrence MS, Lin P, Meier S, Noble MS,  
966                   Saksena G, Voet D, Zhang Hailei, Bernard B, Chambwe N, Dhankani V, Knijnenburg  
967                   T, Kramer R, Leinonen K, Liu Y, Miller M, Reynolds S, Shmulevich I, Thorsson  
968                   Vésteinn, Zhang W, Akbani R, Broom BM, Hegde AM, Ju Z, Kanchi RS, Korkut A, Li  
969                   J, Liang H, Ling S, Liu W, Lu Y, Mills GB, Ng K-S, Rao A, Ryan M, Wang Jing,  
970                   Weinstein JN, Zhang J, Abeshouse A, Armenia J, Chakravarty D, Chatila WK, Bruijn  
971                   I de, Gao J, Gross BE, Heins ZJ, Kundra R, La K, Ladanyi M, Luna A, Nissan MG,  
972                   Ochoa A, Phillips SM, Reznik E, Sanchez-Vega F, Sander C, Schultz N, Sheridan R,  
973                   Sumer SO, Sun Y, Taylor BS, Wang Jiaoajiao, Zhang Hongxin, Anur P, Peto M,

974 Spellman P, Benz C, Stuart JM, Wong CK, Yau C, Hayes DN, Parker JS, Wilkerson  
975 MD, Ally A, Balasundaram M, Bowlby R, Brooks D, Carlsen R, Chuah E, Dhalla N,  
976 Holt R, Jones SJM, Kasaian K, Lee D, Ma Y, Marra MA, Mayo M, Moore RA, Mungall  
977 AJ, Mungall K, Robertson AG, Sadeghi S, Schein JE, Sipahimalani P, Tam A,  
978 Thiessen N, Tse K, Wong T, Berger AC, Beroukhim R, Cherniack AD, Cibulskis C,  
979 Gabriel SB, Gao GF, Ha G, Meyerson M, Schumacher SE, Shih J, Kucherlapati MH,  
980 Kucherlapati RS, Baylin S, Cope L, Danilova L, Bootwalla MS, Lai PH, Maglione DT,  
981 Berg DJVD, Weisenberger DJ, Auman JT, Balu S, Bodenheimer T, Fan C, Hoadley  
982 KA, Hoyle AP, Jefferys SR, Jones CD, Meng S, Mieczkowski PA, Mose LE, Perou  
983 AH, Perou CM, Roach J, Shi Y, Simons JV, Skelly T, Soloway MG, Tan D, Veluvolu  
984 U, Fan H, Hinoue T, Laird PW, Shen H, Zhou W, Bellair M, Chang K, Covington K,  
985 Creighton CJ, Dinh H, Doddapaneni H, Donehower LA, Drummond J, Gibbs RA,  
986 Glenn R, Hale W, Han Y, Hu J, Korchina V, Lee S, Lewis L, Li W, Liu X, Morgan M,  
987 Morton D, Muzny D, Santibanez J, Sheth M, Shinbrot E, Wang L, Wang M, Wheeler  
988 DA, Xi L, Zhao F, Hess J, Appelbaum EL, Bailey M, Cordes MG, Ding L, Fronick CC,  
989 Fulton LA, Fulton RS, Kandoth C, Mardis ER, McLellan MD, Miller CA, Schmidt HK,  
990 Wilson RK, Crain D, Curley E, Gardner J, Lau K, Mallory D, Morris S, Paulauskis J,  
991 Penny R, Shelton C, Shelton T, Sherman M, Thompson E, Yena P, Bowen J,  
992 Gastier-Foster JM, Gerken M, Leraas KM, Lichtenberg TM, Ramirez NC, Wise L,  
993 Zmuda E, Corcoran N, Costello T, Hovens C, Carvalho AL, Carvalho AC de,  
994 Fregnani JH, Longatto-Filho A, Reis RM, Scapulatempo-Neto C, Silveira HCS, Vidal  
995 DO, Burnette A, Eschbacher J, Hermes B, Noss A, Singh R, Anderson ML, Castro  
996 PD, Ittmann M, Huntsman D, Kohl B, Le X, Thorp R, Andry C, Duffy ER, Lyadov V,  
997 Paklina O, Setdikova G, Shabunin A, Tavobilov M, McPherson C, Warnick R,  
998 Berkowitz R, Cramer D, Feltmate C, Horowitz N, Kibel A, Muto M, Raut CP, Malykh  
999 A, Barnholtz-Sloan JS, Barrett W, Devine K, Fulop J, Ostrom QT, Shimmel K,  
1000 Wolinsky Y, Sloan AE, Rose AD, Giuliano F, Goodman M, Karlan BY, Hagedorn CH,  
1001 Eckman J, Harr J, Myers J, Tucker K, Zach LA, Deyarmin B, Hu H, Kvecher L,  
1002 Larson C, Mural RJ, Somiari S, Vicha A, Zelinka T, Bennett J, Iacocca M, Rabeno B,  
1003 Swanson P, Latour M, Lacombe L, Tétu B, Bergeron A, McGraw M, Staugaitis SM,  
1004 Chabot J, Hibshoosh H, Sepulveda A, Su T, Wang T, Potapova O, Voronina O,  
1005 Desjardins L, Mariani O, Roman-Roman S, Sastre X, Stern M-H, Cheng F, Signoretti  
1006 S, Berchuck A, Bigner D, Lipp E, Marks J, McCall S, McLendon R, Secord A, Sharp  
1007 A, Behera M, Brat DJ, Chen A, Delman K, Force S, Khuri F, Magliocca K, Maithel S,  
1008 Olson JJ, Owonikoko T, Pickens A, Ramalingam S, Shin DM, Sica G, Meir EGV,  
1009 Zhang Hongzheng, Eijkenboom W, Gillis A, Korpershoek E, Looijenga L, Oosterhuis  
1010 W, Stoop H, Kessel KE van, Zwarthoff EC, Calatozzolo C, Cappini L, Cuzzubbo S,  
1011 DiMeco F, Finocchiaro G, Mattei L, Perin A, Pollo B, Chen C, Houck J,  
1012 Lohavanichbutr P, Hartmann A, Stoehr C, Stoehr R, Taubert H, Wach S, Wullich B,  
1013 Kyeler W, Murawa D, Wiznerowicz M, Chung K, Edenfield WJ, Martin J, Baudin E,  
1014 Bubley G, Bueno R, Rienzo AD, Richards WG, Kalkanis S, Mikkelsen T, Noushmehr  
1015 H, Scarpace L, Girard N, Aymerich M, Campo E, Giné E, Guillermo AL, Bang NV,  
1016 Hanh PT, Phu BD, Tang Y, Colman H, Eason K, Dottino PR, Martignetti JA, Gabra  
1017 H, Juhl H, Akereolu T, Stepa S, Hoon D, Ahn K, Kang KJ, Beuschlein F, Breggia A,  
1018 Birrer M, Bell D, Borad M, Bryce AH, Castle E, Chandan V, Cheville J, Copland JA,  
1019 Farnell M, Flotte T, Giama N, Ho T, Kendrick M, Kocher J-P, Kopp K, Moser C,  
1020 Nagorney D, O'Brien D, O'Neill BP, Patel T, Petersen G, Que F, Rivera M, Roberts L,  
1021 Smallridge R, Smyrk T, Stanton M, Thompson RH, Torbenson M, Yang JD, Zhang L,  
1022 Brimo F, Ajani JA, Gonzalez AMA, Behrens C, Bondaruk O, Broaddus R, Czerniak B,  
1023 Esmaeli B, Fujimoto J, Gershenwald J, Guo C, Lazar AJ, Logothetis C, Meric-  
1024 Bernstam F, Moran C, Ramondetta L, Rice D, Sood A, Tamboli P, Thompson T,  
1025 Troncoso P, Tsao A, Wistuba I, Carter C, Haydu L, Hersey P, Jakrot V, Kakavand H,  
1026 Kefford R, Lee K, Long G, Mann G, Quinn M, Saw R, Scolyer R, Shannon K, Spillane  
1027 A, Stretch J, Synott M, Thompson J, Wilmott J, Al-Ahmadi H, Chan TA, Ghossein R,  
1028 Gopalan A, Levine DA, Reuter V, Singer S, Singh B, Tien NV, Broudy T, Mirsaidi C,

- 1029 Nair P, Drwiega P, Miller J, Smith J, Zaren H, Park J-W, Hung NP, Kebebew E,  
1030 Linehan WM, Metwalli AR, Pacak K, Pinto PA, Schiffman M, Schmidt LS, Vocke CD,  
1031 Wentzzenen N, Worrell R, Yang H, Moncrieff M, Goparaju C, Melamed J, Pass H,  
1032 Botnariuc N, Caraman I, Cernat M, Chemencedji I, Clipca A, Doruc S, Gorincioi G,  
1033 Mura S, Pirtac M, Stancul I, Tcaciu D, Albert M, Alexopoulos I, Arnaout A, Bartlett J,  
1034 Engel J, Gilbert S, Parfitt J, Sekhon H, Thomas G, Rassl DM, Rintoul RC, Bifulco C,  
1035 Tamakawa R, Urba W, Hayward N, Timmers H, Antenucci A, Facciolo F, Grazi G,  
1036 Marino M, Merola R, Krijger R de, Gimenez-Roqueplo A-P, Piché A, Chevalier S,  
1037 McKercher G, Birsoy K, Barnett G, Brewer C, Farver C, Naska T, Pennell NA,  
1038 Raymond D, Schilero C, Smolenski K, Williams F, Morrison C, Borgia JA, Liptay MJ,  
1039 Pool M, Seder CW, Junker K, Omberg L, Dinkin M, Manikhas G, Alvaro D, Bragazzi  
1040 MC, Cardinale V, Carpino G, Gaudio E, Chesla D, Cottingham S, Dubina M,  
1041 Moiseenko F, Dhanasekaran R, Becker K-F, Janssen K-P, Slotta-Huspenina J,  
1042 Abdel-Rahman MH, Aziz D, Bell S, Cebulla CM, Davis A, Duell R, Elder JB, Hilty J,  
1043 Kumar B, Lang J, Lehman NL, Mandt R, Nguyen P, Pilarski R, Rai K, Schoenfield L,  
1044 Senecal K, Wakely P, Hansen P, Lechan R, Powers J, Tischler A, Grizzle WE,  
1045 Sexton KC, Kastl A, Henderson J, Porten S, Waldmann J, Fassnacht M, Asa SL,  
1046 Schadendorf D, Couce M, Graefen M, Huland H, Sauter G, Schlomm T, Simon R,  
1047 Tennstedt P, Olabode O, Nelson M, Bathe O, Carroll PR, Chan JM, Disaia P, Glenn  
1048 P, Kelley RK, Landen CN, Phillips J, Prados M, Simko J, Smith-McCune K,  
1049 Vandenberg S, Roggin K, Fehrenbach A, Kendler A, Sifri S, Steele R, Jimeno A,  
1050 Carey F, Forgie I, Mannelli M, Carney M, Hernandez B, Campos B, Herold-Mende C,  
1051 Jungk C, Unterberg A, Deimling A von, Bossler A, Galbraith J, Jacobus L, Knudson  
1052 M, Knutson T, Ma D, Milhem M, Sigmund R, Godwin AK, Madan R, Rosenthal HG,  
1053 Adebamowo C, Adebamowo SN, Boussioutas A, Beer D, Giordano T, Mes-Masson  
1054 A-M, Saad F, Bocklage T, Landrum L, Mannel R, Moore K, Moxley K, Postier R,  
1055 Walker J, Zuna R, Feldman M, Valdivieso F, Dhir R, Luketich J, Pinero EMM,  
1056 Quintero-Aguilo M, Carlotti CG, Santos JSD, Kemp R, Sankarankutty A, Tirapelli D,  
1057 Catto J, Agnew K, Swisher E, Creaney J, Robinson B, Shelley CS, Godwin EM,  
1058 Kendall S, Shipman C, Bradford C, Carey T, Haddad A, Moyer J, Peterson L, Prince  
1059 M, Rozek L, Wolf G, Bowman R, Fong KM, Yang I, Korst R, Rathmell WK,  
1060 Fantacone-Campbell JL, Hooke JA, Kovatich AJ, Shriver CD, DiPersio J, Drake B,  
1061 Govindan R, Heath S, Ley T, Tine BV, Westervelt P, Rubin MA, Lee JI, Arends ND,  
1062 Mariamidze A, Stuart JM, Benz CC, Laird PW. 2018. Cell-of-Origin Patterns  
1063 Dominate the Molecular Classification of 10,000 Tumors from 33 Types of Cancer.  
1064 *Cell* **173**:291-304.e6. doi:10.1016/j.cell.2018.03.022  
1065 Horoszewicz JS, Leong SS, Kawinski E, Karr JP, Rosenthal H, Chu TM, Mirand EA, Murphy  
1066 GP. 1983. LNCaP model of human prostatic carcinoma. *Cancer Res* **43**:1809–1818.  
1067 Hu Y, Gu Y, Wang H, Huang Y, Zou YM. 2015. Integrated network model provides new  
1068 insights into castration-resistant prostate cancer. *Sci Rep* **5**:17280.  
1069 doi:10.1038/srep17280  
1070 Iorio F, Knijnenburg TA, Vis DJ, Bignell GR, Menden MP, Schubert M, Aben N, Gonçalves  
1071 E, Barhorpe S, Lightfoot H, Cokelaer T, Greninger P, van Dyk E, Chang H, de Silva  
1072 H, Heyn H, Deng X, Egan RK, Liu Q, Mironenko T, Mitropoulos X, Richardson L,  
1073 Wang J, Zhang T, Moran S, Sayols S, Soleimani M, Tamborero D, Lopez-Bigas N,  
1074 Ross-Macdonald P, Esteller M, Gray NS, Haber DA, Stratton MR, Benes CH,  
1075 Wessels LFA, Saez-Rodriguez J, McDermott U, Garnett MJ. 2016. A Landscape of  
1076 Pharmacogenomic Interactions in Cancer. *Cell* **166**:740–754.  
1077 doi:10.1016/j.cell.2016.06.017  
1078 Iwai A, Bourboulia D, Mollapour M, Jensen-Taubman S, Lee S, Donnelly AC, Yoshida S,  
1079 Miyajima N, Tsutsumi S, Smith AK, Sun D, Wu X, Blagg BS, Trepel JB, Stetler-  
1080 Stevenson WG, Neckers L. 2012. Combined inhibition of Wee1 and Hsp90 activates  
1081 intrinsic apoptosis in cancer cells. *Cell Cycle Georget Tex* **11**:3649–3655.  
1082 doi:10.4161/cc.21926

- 1083 Johnson BE, Whang-Peng J, Naylor SL, Zbar B, Brauch H, Lee E, Simmons A, Russell E,  
1084 Nam MH, Gazdar AF. 1989. Retention of chromosome 3 in extrapulmonary small cell  
1085 cancer shown by molecular and cytogenetic studies. *J Natl Cancer Inst* **81**:1223–  
1086 1228. doi:10.1093/jnci/81.16.1223
- 1087 Kaighn ME, Narayan KS, Ohnuki Y, Lechner JF, Jones LW. 1979. Establishment and  
1088 characterization of a human prostatic carcinoma cell line (PC-3). *Invest Urol* **17**:16–  
1089 23.
- 1090 Kauffman SA. 1969. Metabolic stability and epigenesis in randomly constructed genetic nets.  
1091 *J Theor Biol* **22**:437–467.
- 1092 Kholodenko B, Schuster S, Rohwer JM, Cascante M, Westerhoff HV. 1995. Composite  
1093 control of cell function: metabolic pathways behaving as single control units. *FEBS Lett*  
1094 **368**.
- 1095 Korenchuk S, Lehr JE, MClean L, Lee YG, Whitney S, Vessella R, Lin DL, Pienta KJ. 2001.  
1096 VCaP, a cell-based model system of human prostate cancer. *Vivo Athens Greece*  
1097 **15**:163–168.
- 1098 Korotkevich G, Sukhov V, Sergushichev A. 2016. Fast gene set enrichment analysis.  
1099 *bioRxiv*. doi:10.1101/060012
- 1100 Korzybski A. 1995. Science and sanity: an introduction to non-Aristotelian systems and  
1101 general semantics, 5. ed., 3. print. ed. Brooklyn, N.Y: Inst. of General Semantics.
- 1102 Krug K, Mertins P, Zhang B, Hornbeck P, Raju R, Ahmad R, Szucs M, Mundt F, Forestier D,  
1103 Jane-Valbuena J, Keshishian H, Gillette MA, Tamayo P, Mesirov JP, Jaffe JD, Carr  
1104 S, Mani DR. 2019. A Curated Resource for Phosphosite-specific Signature Analysis  
1105 \*[S]. *Mol Cell Proteomics* **18**:576–593. doi:10.1074/mcp.TIR118.000943
- 1106 Krzyszczyk P, Acevedo A, Davidoff EJ, Timmins LM, Marrero-Berrios I, Patel M, White C,  
1107 Lowe C, Sherba JJ, Hartmanshenn C, O'Neill KM, Balter ML, Fritz ZR, Androulakis  
1108 IP, Schloss RS, Yarmush ML. 2018. The growing role of precision and personalized  
1109 medicine for cancer treatment. *Technology* **6**:79–100.  
1110 doi:10.1142/S2339547818300020
- 1111 Kunderfranco P, Mello-Grand M, Cangemi R, Pellini S, Mensah A, Albertini V, Malek A,  
1112 Chiorino G, Catapano CV, Carbone GM. 2010. ETS transcription factors control  
1113 transcription of EZH2 and epigenetic silencing of the tumor suppressor gene Nkx3.1  
1114 in prostate cancer. *PLoS One* **5**:e10547. doi:10.1371/journal.pone.0010547
- 1115 Kuperstein I, Bonnet E, Nguyen H-A, Cohen D, Viara E, Grieco L, Fourquet S, Calzone L,  
1116 Russo C, Kondratova M, Dutreix M, Barillot E, Zinovyev A. 2015. Atlas of Cancer  
1117 Signalling Network: a systems biology resource for integrative analysis of cancer  
1118 data with Google Maps. *Oncogenesis* **4**:e160. doi:10.1038/oncsis.2015.19
- 1119 Lai SL, Brauch H, Knutson T, Johnson BE, Nau MM, Mitsudomi T, Tsai CM, Whang-Peng J,  
1120 Zbar B, Kaye FJ. 1995. Molecular genetic characterization of neuroendocrine lung  
1121 cancer cell lines. *Anticancer Res* **15**:225–232.
- 1122 Le B, Powers GL, Tam YT, Schumacher N, Malinowski RL, Steinke L, Kwon G, Marker PC.  
1123 2017. Multi-drug loaded micelles delivering chemotherapy and targeted therapies  
1124 directed against HSP90 and the PI3K/AKT/mTOR pathway in prostate cancer. *PLOS  
1125 ONE* **12**:e0174658. doi:10.1371/journal.pone.0174658
- 1126 Le Novère N. 2015. Quantitative and logic modelling of molecular and gene networks. *Nat  
1127 Rev Genet* **16**:146–58. doi:10.1038/nrg3885
- 1128 Lé S, Josse J, Husson F. 2008. FactoMineR: An R Package for Multivariate Analysis. *J Stat  
1129 Softw* **25**:1–18. doi:10.18637/jss.v025.i01
- 1130 Liberzon A, Birger C, Thorvaldsdóttir H, Ghandi M, Mesirov JP, Tamayo P. 2015. The  
1131 Molecular Signatures Database (MSigDB) hallmark gene set collection. *Cell Syst*  
1132 **1**:417–425. doi:10.1016/j.cels.2015.12.004
- 1133 Madani Tonekaboni SA, Soltan Ghoraie L, Manem VSK, Haibe-Kains B. 2018. Predictive  
1134 approaches for drug combination discovery in cancer. *Brief Bioinform* **19**:263–276.  
1135 doi:10.1093/bib/bbw104
- 1136 Malik-Sheriff RS, Glont M, Nguyen TVN, Tiwari K, Roberts MG, Xavier A, Vu MT, Men J,  
1137 Maire M, Kananathan S, Fairbanks EL, Meyer JP, Arankalle C, Varusai TM, Knight-

- 1138 Schrijver V, Li L, Dueñas-Roca C, Dass G, Keating SM, Park YM, Buso N, Rodriguez  
1139 N, Hucka M, Hermjakob H. 2019. BioModels—15 years of sharing computational  
1140 models in life science. *Nucleic Acids Res* gkz1055. doi:10.1093/nar/gkz1055
- 1141 Marshall CH, Fu W, Wang H, Baras AS, Lotan TL, Antonarakis ES. 2019. Prevalence of  
1142 DNA repair gene mutations in localized prostate cancer according to clinical and  
1143 pathologic features: association of Gleason score and tumor stage. *Prostate Cancer*  
1144 *Prostatic Dis* **22**:59–65. doi:10.1038/s41391-018-0086-1
- 1145 Martignetti L, Calzone L, Bonnet E, Barillot E, Zinovyev A. 2016. ROMA: Representation and  
1146 Quantification of Module Activity from Target Expression Data. *Front Genet* **7**:18.  
1147 doi:10.3389/fgene.2016.00018
- 1148 Menden MP, Wang D, Mason MJ, Szalai B, Bulusu KC, Guan Y, Yu T, Kang J, Jeon M,  
1149 Wolfinger R, Nguyen T, Zaslavskiy M, Jang IS, Ghazouli Z, Ahsen ME, Vogel R, Neto  
1150 EC, Norman T, Tang EKY, Garnett MJ, Veroli GYD, Fawell S, Stolovitzky G, Guinney  
1151 J, Dry JR, Saez-Rodriguez J. 2019. Community assessment to advance  
1152 computational prediction of cancer drug combinations in a pharmacogenomic screen.  
1153 *Nat Commun* **10**:2674. doi:10.1038/s41467-019-09799-2
- 1154 Molinari C, Marisi G, Passardi A, Matteucci L, De Maio G, Ulivi P. 2018. Heterogeneity in  
1155 Colorectal Cancer: A Challenge for Personalized Medicine? *Int J Mol Sci* **19**:3733.  
1156 doi:10.3390/ijms19123733
- 1157 Montagud A, Ponce-de-Leon M, Valencia A. 2021. Systems biology at the giga-scale: Large  
1158 multiscale models of complex, heterogeneous multicellular systems. *Curr Opin Syst*  
1159 *Biol* **28**:100385. doi:10.1016/j.coisb.2021.100385
- 1160 Montagud A, Traynard P, Martignetti L, Bonnet E, Barillot E, Zinovyev A, Calzone L. 2017.  
1161 Conceptual and computational framework for logical modelling of biological networks  
1162 deregulated in diseases. *Brief Bioinform* bbx163. doi:10.1093/bib/bbx163
- 1163 Ozsvári B, Puskás LG, Nagy LI, Kanizsai I, Gyuris M, Madácsi R, Fehér LZ, Gerő D, Szabó  
1164 C. 2010. A cell-microelectronic sensing technique for the screening of cytoprotective  
1165 compounds. *Int J Mol Med* **25**:525–530. doi:10.3892/ijmm\_00000373
- 1166 Pacey S, Wilson RH, Walton M, Eatock MM, Hardcastle A, Zetterlund A, Arkenau H-T,  
1167 Moreno-Farre J, Banerji U, Roels B, Peachey H, Aherne W, de Bono JS, Raynaud F,  
1168 Workman P, Judson I. 2011. A phase I study of the heat shock protein 90 inhibitor  
1169 alvespimycin (17-DMAG) given intravenously to patients with advanced solid tumors.  
1170 *Clin Cancer Res Off J Am Assoc Cancer Res* **17**:1561–1570. doi:10.1158/1078-  
1171 0432.CCR-10-1927
- 1172 Perfetto L, Briganti L, Calderone A, Cerquone Perpetuini A, Iannuccelli M, Langone F, Licata  
1173 L, Marinkovic M, Mattioni A, Pavlidou T, Peluso D, Petrilli LL, Pirrò S, Posca D,  
1174 Santonicò E, Silvestri A, Spada F, Castagnoli L, Cesareni G. 2016. SIGNOR: a  
1175 database of causal relationships between biological entities. *Nucleic Acids Res*  
1176 **44**:D548–D554. doi:10.1093/nar/gkv1048
- 1177 Ponce-de-Leon M, Montagud A, Akasiadis C, Schreiber J, Ntiniakou T, Valencia A. 2021.  
1178 Optimizing dosage-specific treatments in a multi-scale model of a tumor growth.  
1179 *bioRxiv* 2021.12.17.473136. doi:10.1101/2021.12.17.473136
- 1180 Ponce-de-Leon M, Montagud A, Noel V, Pradas G, Meert A, Barillot E, Calzone L, Valencia  
1181 A. 2022. PhysiBoSS 2.0: a sustainable integration of stochastic Boolean and agent-  
1182 based modelling frameworks. *bioRxiv* 2022.01.06.468363.  
1183 doi:10.1101/2022.01.06.468363
- 1184 Raynaud FI, Eccles SA, Patel S, Alix S, Box G, Chuckowree I, Folkes A, Gowan S, De  
1185 Haven Brandon A, Di Stefano F, Hayes A, Henley AT, Lensun L, Pergl-Wilson G,  
1186 Robson A, Saghir N, Zhyvoloup A, McDonald E, Sheldrake P, Shuttleworth S, Valenti  
1187 M, Wan NC, Clarke PA, Workman P. 2009. Biological properties of potent inhibitors  
1188 of class I phosphatidylinositide 3-kinases: from PI-103 through PI-540, PI-620 to the  
1189 oral agent GDC-0941. *Mol Cancer Ther* **8**:1725–1738. doi:10.1158/1535-7163.MCT-  
1190 08-1200
- 1191 Remy E, Rebouissou S, Chaouiya C, Zinovyev A, Radvanyi F, Calzone L. 2015. A Modeling  
1192 Approach to Explain Mutually Exclusive and Co-Occurring Genetic Alterations in

- 1193 Bladder Tumorigenesis. *Cancer Res* **75**:4042–4052. doi:10.1158/0008-5472.CAN-  
1194 15-0602

1195 Ren G, Baritaki S, Marathe H, Feng J, Park S, Beach S, Bazeley PS, Beshir AB, Fenteany  
1196 G, Mehra R, Daignault S, Al-Mulla F, Keller E, Bonavida B, de la Serna I, Yeung KC.  
1197 2012. Polycomb protein EZH2 regulates tumor invasion via the transcriptional  
1198 repression of the metastasis suppressor RKIP in breast and prostate cancer. *Cancer  
1199 Res* **72**:3091–3104. doi:10.1158/0008-5472.CAN-11-3546

1200 Rivas-Barragan D, Mubeen S, Bernat FG, Hofmann-Apitius M, Domingo-Fernández D. 2020.  
1201 Drug2ways: Reasoning over causal paths in biological networks for drug discovery.  
1202 *PLOS Comput Biol* **16**:e1008464. doi:10.1371/journal.pcbi.1008464

1203 Robinson D, Van Allen EM, Wu Y-M, Schultz N, Lonigro RJ, Mosquera J-M, Montgomery B,  
1204 Taplin M-E, Pritchard CC, Attard G, Beltran H, Abida W, Bradley RK, Vinson J, Cao  
1205 X, Vats P, Kunju LP, Hussain M, Feng FY, Tomlins SA, Cooney KA, Smith DC,  
1206 Brennan C, Siddiqui J, Mehra R, Chen Y, Rathkopf DE, Morris MJ, Solomon SB,  
1207 Durack JC, Reuter VE, Gopalan A, Gao J, Loda M, Lis RT, Bowden M, Balk SP,  
1208 Gaviola G, Sougnez C, Gupta M, Yu EY, Mostaghel EA, Cheng HH, Mulcahy H, True  
1209 LD, Plymate SR, Dvinge H, Ferraldeschi R, Flohr P, Miranda S, Zafeiriou Z, Tunariu  
1210 N, Mateo J, Perez-Lopez R, Demichelis F, Robinson BD, Schiffman M, Nanus DM,  
1211 Tagawa ST, Sigaras A, Eng KW, Elemento O, Sboner A, Heath EI, Scher HI, Pienta  
1212 KJ, Kantoff P, de Bono JS, Rubin MA, Nelson PS, Garraway LA, Sawyers CL,  
1213 Chinnaiyan AM. 2015. Integrative Clinical Genomics of Advanced Prostate Cancer.  
1214 *Cell* **161**:1215–1228. doi:10.1016/j.cell.2015.05.001

1215 Rosenblueth A, Wiener N. 1945. The Role of Models in Science. *Philos Sci* **12**:316–321.  
1216 doi:10.1086/286874

1217 Saadatpour A, Albert R. 2013. Boolean modeling of biological regulatory networks: a  
1218 methodology tutorial. *Methods San Diego Calif* **62**:3–12.  
1219 doi:10.1016/j.ymeth.2012.10.012

1220 Saez-Rodriguez J, Alexopoulos LG, Epperlein J, Samaga R, Lauffenburger DA, Klamt S,  
1221 Sorger PK. 2009. Discrete logic modelling as a means to link protein signalling  
1222 networks with functional analysis of mammalian signal transduction. *Mol Syst Biol* **5**.  
1223 doi:10.1038/msb.2009.87

1224 Saez-Rodriguez J, Blüthgen N. 2020. Personalized signaling models for personalized  
1225 treatments. *Mol Syst Biol* **16**:e9042. doi:10.15252/msb.20199042

1226 Saxena G, Ponce-de-Leon M, Montagud A, Vicente Dorca D, Valencia A. 2021. BioFVM-X:  
1227 An MPI+OpenMP 3-D Simulator for Biological Systems In: Cinquemani E, Paulevé L,  
1228 editors. Computational Methods in Systems Biology, Lecture Notes in Computer  
1229 Science. Cham: Springer International Publishing. pp. 266–279. doi:10.1007/978-3-  
1230 030-85633-5\_18

1231 Schopf FH, Biebl MM, Buchner J. 2017. The HSP90 chaperone machinery. *Nat Rev Mol Cell  
1232 Biol* **18**:345–360. doi:10.1038/nrm.2017.20

1233 Scott LJ. 2018. Enzalutamide: A Review in Castration-Resistant Prostate Cancer. *Drugs*  
1234 **78**:1913–1924. doi:10.1007/s40265-018-1029-9

1235 Shorning BY, Dass MS, Smalley MJ, Pearson HB. 2020. The PI3K-AKT-mTOR Pathway and  
1236 Prostate Cancer: At the Crossroads of AR, MAPK, and WNT Signaling. *Int J Mol Sci*  
1237 **21**:4507. doi:10.3390/ijms21124507

1238 Sible JC, Tyson JJ. 2007. Mathematical modeling as a tool for investigating cell cycle control  
1239 networks. *Methods San Diego Calif* **41**:238–247. doi:10.1016/j.ymeth.2006.08.003

1240 Solly K, Wang X, Xu X, Strulovici B, Zheng W. 2004. Application of Real-Time Cell Electronic  
1241 Sensing (RT-CES) Technology to Cell-Based Assays. *ASSAY Drug Dev Technol*  
1242 **2**:363–372. doi:10.1089/adt.2004.2.363

1243 Sramkoski RM, Pretlow TG, Giaconia JM, Pretlow TP, Schwartz S, Sy MS, Marengo SR,  
1244 Rhim JS, Zhang D, Jacobberger JW. 1999. A new human prostate carcinoma cell  
1245 line, 22Rv1. *In Vitro Cell Dev Biol Anim* **35**:403–409. doi:10.1007/s11626-999-0115-4

1246 St John J, Powell K, Conley-Lacomb MK, Chinni SR. 2012. TMPRSS2-ERG Fusion Gene  
1247 Expression in Prostate Tumor Cells and Its Clinical and Biological Significance in

- 1248 Prostate Cancer Progression. *J Cancer Sci Ther* **4**:94–101. doi:10.4172/1948-  
1249 5956.1000119

1250 Stoll G, Caron B, Viara E, Dugourd A, Zinovyev A, Naldi A, Kroemer G, Barillot E, Calzone L.  
1251 2017. MaBoSS 2.0: an environment for stochastic Boolean modeling. *Bioinformatics*  
1252 **33**:2226–2228. doi:10.1093/bioinformatics/btx123

1253 Stoll G, Viara E, Barillot E, Calzone L. 2012. Continuous time Boolean modeling for  
1254 biological signaling: application of Gillespie algorithm. *BMC Syst Biol* **6**:116.  
1255 doi:10.1186/1752-0509-6-116

1256 Stone KR, Mickey DD, Wunderli H, Mickey GH, Paulson DF. 1978. Isolation of a human  
1257 prostate carcinoma cell line (DU 145). *Int J Cancer* **21**:274–281.  
1258 doi:10.1002/ijc.2910210305

1259 Szebeni GJ, Balázs Á, Madarász I, Pócz G, Ayaydin F, Kanizsai I, Fajka-Boja R, Alföldi R,  
1260 Hackler Jr. L, Puskás LG. 2017. Achiral Mannich-Base Curcumin Analogs Induce  
1261 Unfolded Protein Response and Mitochondrial Membrane Depolarization in PANC-1  
1262 Cells. *Int J Mol Sci* **18**:2105. doi:10.3390/ijms18102105

1263 The Cancer Genome Atlas Research Network. 2015. The Molecular Taxonomy of Primary  
1264 Prostate Cancer. *Cell* **163**:1011–1025. doi:10.1016/j.cell.2015.10.025

1265 Thomas R. 1973. Boolean formalization of genetic control circuits. *J Theor Biol* **42**:563–585.  
1266 doi:10.1016/0022-5193(73)90247-6

1267 Toth R, Schiffmann H, Hube-Magg C, Büscheck F, Höflmayer D, Weidemann S, Lebok P,  
1268 Fraune C, Minner S, Schlomm T, Sauter G, Plass C, Assenov Y, Simon R, Meiners  
1269 J, Gerhäuser C. 2019. Random forest-based modelling to detect biomarkers for  
1270 prostate cancer progression. *Clin Epigenetics* **11**:148. doi:10.1186/s13148-019-0736-  
1271 8

1272 Traynard P, Fauré A, Fages F, Thieffry D. 2016. Logical model specification aided by model-  
1273 checking techniques: application to the mammalian cell cycle regulation. *Bioinforma  
1274 Oxf Engl* **32**:i772–i780. doi:10.1093/bioinformatics/btw457

1275 Türei D, Korcsmáros T, Saez-Rodriguez J. 2016. OmniPath: guidelines and gateway for  
1276 literature-curated signaling pathway resources. *Nat Methods* **13**:966–967.  
1277 doi:10.1038/nmeth.4077

1278 Türei D, Valdeolivas A, Gul L, Palacio-Escat N, Klein M, Ivanova O, Ölbei M, Gábor A, Theis  
1279 F, Módos D, Korcsmáros T, Saez-Rodriguez J. 2021. Integrated intra- and  
1280 intercellular signaling knowledge for multicellular omics analysis. *Mol Syst Biol* **17**.  
1281 doi:10.15252/msb.20209923

1282 Tyson JJ, Laometsachit T, Kraikivski P. 2019. Modeling the dynamic behavior of biochemical  
1283 regulatory networks. *J Theor Biol* **462**:514–527. doi:10.1016/j.jtbi.2018.11.034

1284 Väremo L, Nielsen J, Nookaew I. 2013. Enriching the gene set analysis of genome-wide  
1285 data by incorporating directionality of gene expression and combining statistical  
1286 hypotheses and methods. *Nucleic Acids Res* **41**:4378–4391. doi:10.1093/nar/gkt111

1287 Webber MM, Bello D, Kleinman HK, Wartinger DD, Williams DE, Rhim JS. 1996. Prostate  
1288 specific antigen and androgen receptor induction and characterization of an  
1289 immortalized adult human prostatic epithelial cell line. *Carcinogenesis* **17**:1641–1646.  
1290 doi:10.1093/carcin/17.8.1641

1291 Wishart DS, Feunang YD, Guo AC, Lo EJ, Marcu A, Grant JR, Sajed T, Johnson D, Li C,  
1292 Sayeeda Z, Assempour N, lynkkaran I, Liu Y, Maciejewski A, Gale N, Wilson A, Chin  
1293 L, Cummings R, Le D, Pon A, Knox C, Wilson M. 2018. DrugBank 5.0: a major  
1294 update to the DrugBank database for 2018. *Nucleic Acids Res* **46**:D1074–D1082.  
1295 doi:10.1093/nar/gkx1037

1296 Yang W, Freeman MR, Kyprianou N. 2018. Personalization of prostate cancer therapy  
1297 through phosphoproteomics. *Nat Rev Urol* **15**:483–497. doi:10.1038/s41585-018-  
1298 0014-0

1299 Zhan M, Deng Y, Zhao L, Yan G, Wang F, Tian Y, Zhang L, Jiang H, Chen Y. 2017. Design,  
1300 Synthesis, and Biological Evaluation of Dimorpholine Substituted Thienopyrimidines  
1301 as Potential Class I PI3K/mTOR Dual Inhibitors. *J Med Chem.*  
1302 doi:10.1021/acs.jmedchem.7b00357

1303

1304

## 1305 Tables and their legends

1306 Table 1: List of selected nodes, their corresponding genes and drugs that were included in  
 1307 the drug analysis of the models tailored for TCGA patients and LNCaP cell line.

Node	Gene	Compound / Inhibitor name	Clinical stage	Source
AKT	AKT1, AKT2, AKT3	PI-103	Preclinical	Drug Bank
		Enzastaurin	Phase 3	Drug Bank
		Archexin, Pictilisib	Phase 2	Drug Bank
AR	AR	Abiraterone, Enzalutamide, Formestane, Testosterone propionate	Approved	Drug Bank
		5alpha-androstan-3beta-ol	Preclinical	Drug Bank
Caspase8	CASP8	Bardoxolone	Preclinical	Drug Bank
cFLAR	CFLAR	-	-	-
EGFR	EGFR	Afatinib, Osimertinib, Neratinib, Erlotinib, Gefitinib	Approved	Drug Bank
		Varlitinib	Phase 3	Drug Bank
		Olmutinib, Pelitinib	Phase 2	Drug Bank
ERK	MAPK1	Isoprenaline	Approved	Drug Bank
		Perifosine	Phase 3	Drug Bank
		Turpentine, SB220025, Olomoucine,	Preclinical	Drug Bank

		Phosphonothreonine		
MAPK3, MAPK1	Arsenic trioxide	Approved	Drug Bank	
	Ulixertinib, Seliciclib	Phase 2	Drug Bank	
	Purvalanol	Preclinical	Drug Bank	
	Sulindac, Cholecystokinin	Approved	Drug Bank	
MAPK3	5-iodotubercidin	Preclinical	Drug Bank	
GLUT1	SLC2A1	Resveratrol	Phase 4	Drug Bank
HIF-1	HIF1A	CAY-10585	Preclinical	Drug Bank
HSPs	HSP90AA1, HSP90AB1, HSP90B1, HSPA1A, HSPA1B, HSPB1	Cladribine	Approved	Drug Bank
		17-DMAG	Phase 2	Drug Bank
		NMS-E973	Preclinical	Drug Bank
MEK1_2	MAP2K1, MAP2K2	Trametinib, Selumetinib	Approved	Drug Bank
		Perifosine	Phase 3	Drug Bank
		PD184352 (CI-1040)	Phase 2	Drug Bank
MYC_MAX	complex of MYC and MAX	10058-F4 (for MAX)	Preclinical	Drug Bank
p14ARF	CDKN2A	-	-	-
PI3K	PIK3CA, PIK3CB, PIK3CG, PIK3CD,	PI-103	Preclinical	Drug Bank
		Pictilisib	Phase 2	Drug Bank

	PIK3R1, PIK3R2, PIK3R3, PIK3R4, PIK3R5, PIK3R6, PIK3C2A, PIK3C2B, PIK3C2G, PIK3C3			
ROS	NOX1, NOX3, NOX4	Fostamatinib	Approved	Drug Bank
	NOX2	Dextromethorphan	Approved	Drug Bank
		Tetrahydroisoquinoline (CHEMBL3733336 , CHEMBL3347550, CHEMBL3347551)	Preclinical	ChEMBL
SPOP	SPOP	-	-	-
TERT	TERT	Grn163I	Phase 2	Drug Bank
		BIBR 1532	Preclinical	ChEMBL

1308

1309

## Figure titles and their legends:

**Figure 1: Workflow to build patient-specific Boolean models and to uncover personalised drug treatments from present work.** We gathered data from Fumiā and Martins (2013) Boolean model, Omnipath (Türei et al., 2021) and pathways identified with ROMA (Martignetti et al., 2016) on the TCGA data to build a prostate-specific prior knowledge network. This network was manually converted into a prostate Boolean model that could be stochastically simulated using MaBoSS (Stoll et al., 2017) and tailored to different TCGA and GDSC datasets using our PROFILE tool to have personalised Boolean models. Then, we studied all the possible single and double mutants on these tailored models using our logical pipeline of tools (Montagud et al., 2017). Using these personalised models and our PROFILE\_v2 tool presented in this work, we obtained tailored drug simulations and drug treatments for 488 TCGA patients and eight prostate cell lines. Lastly, we performed drug-dose experiments on a shortlist of candidate drugs that were particularly interesting in the LNCaP prostate cell line. Created with BioRender.com.

**Figure 2: Prostate Boolean model used in present work.** Nodes (ellipses) represent biological entities, and arcs are positive (green) or negative (red) influences of one entity on another one. Orange rectangles correspond to inputs (from left to right: Epithelial Growth Factor (EGF), Fibroblast Growth Factor (FGF), Transforming Growth Factor beta (TGFbeta), Nutrients, Hypoxia, Acidosis, Androgen, fused\_event, Tumour Necrosis Factor alpha (TNFalpha), SPOP, Carcinogen) and dark blue rectangles to outputs that represent biological phenotypes (from left to right: Proliferation, Migration, Invasion, Metastasis, Apoptosis, DNA\_repair), the read-outs of the model. This network is available to be inspected as a Cytoscape file in the Supplementary File 1.

**Figure 3: Prostate Boolean model MaBoSS simulations.** (A) The model was simulated with all initial inputs set to 0 and all other variables random. All phenotypes are 0 at the end of the simulations, which should be understood as a quiescent state, where neither proliferation nor apoptosis is active. (B) The model was simulated with growth factors (*EGF* and *FGF*), *Nutrients* and *Androgen* ON. (C) The model was simulated with *Carcinogen*, *Androgen*, *TNFalpha*, *Acidosis*, and *Hypoxia* ON.

**Figure 4: Associations between simulations and Gleason grades (GG).** A) Centroids of the Principal Component Analysis of the samples according to their Gleason grades (GG). The personalisation recipe used was mutations and copy number alterations (CNA) as discrete data and RNAseq as continuous data. Density plots of *Proliferation* (B) and *Apoptosis* (C) scores according to GG; each vignette corresponds to a specific sub-cohort with a given GG. Kruskal-Wallis rank sum test across GG is significant for Proliferation (p-value=0.00207) and Apoptosis (p-value=2.83E-6).

**Figure 5: Phenotype score variations and synergy upon combined ERK and MYC\_MAX (A and C) and HSPs and PI3K (B and D) inhibition under EGF growth condition.** Proliferation score variation (A) and Bliss Independence synergy score (C) with increased node activation of nodes ERK and MYC\_MAX. Proliferation score variation (B) and Bliss Independence synergy score (D) with increased node activation of nodes HSPs and PI3K. Bliss Independence synergy score < 1 is characteristic of drug synergy, grey colour means one of the drugs is absent, and thus no synergy score is available.

1353 **Figure 6: Model-targeting drugs' sensitivities across prostate cell lines.** GDSC z-score  
1354 was obtained for all the drugs targeting genes included in the model for all the prostate cell  
1355 lines in GDSC. Negative values mean that the cell line is more sensitive to the drug. Drugs  
1356 included in Table 1 were highlighted. "Other targets" are drugs targeting model-related  
1357 genes that are not part of Table 1.

1358 **Figure 7: Cell viability assay determined by the fluorescent resazurin after a 48-hours**  
1359 **incubation showed a dose-dependent response to different inhibitors.** A) Cell viability  
1360 assay of LNCaP cell line response to 17-DMAG HSP90 inhibitor. B) Cell viability assay of  
1361 LNCaP cell line response to PI-103 PI3K/AKT pathway inhibitor. C) Cell viability assay of  
1362 LNCaP cell line response to NMS-E973 HSP90 inhibitor. D) Cell viability assay of LNCaP  
1363 cell line response to Pictilisib PI3K/AKT pathway inhibitor. Concentrations of drugs were  
1364 selected to capture their drug-dose response curves. The concentrations for the NMS-E973  
1365 are different from the rest as this drug is more potent than the rest (see Material and  
1366 methods).

1367 **Figure 8: Hsp90 inhibitors resulted in dose-dependent changes in the LNCaP cell line**  
1368 **growth.** A) Real-time cell electronic sensing (RT-CES) cytotoxicity assay of Hsp90 inhibitor,  
1369 17-DMAG, that uses the Cell Index as a measurement of the cell growth rate (see the  
1370 Material and Methods section). The yellow dotted line represents the 17-DMAG addition. B)  
1371 RT-CES cytotoxicity assay of Hsp90 inhibitor, NMS-E973. The yellow dotted line represents  
1372 the NMS-E973 addition.

1373 **Figure 9: PI3K/AKT pathway inhibition with different PI3K/AKT inhibitors shows the**  
1374 **dose-dependent response in LNCaP cell line growth.** A) Real-time cell electronic sensing  
1375 (RT-CES) cytotoxicity assay of PI3K/AKT pathway inhibitor, PI-103, that uses the Cell Index  
1376 as a measurement of the cell growth rate (see the Material and Methods section). The yellow  
1377 dotted line represents the PI-103 addition. B) RT-CES cytotoxicity assay of PI3K/AKT  
1378 pathway inhibitor, Pictilisib. The yellow dotted line represents the Pictilisib addition.

## 1379 Appendix, Supplementary Files, Source code and 1380 Source data files

1381 Appendix 1, a document with supplemental analyses, extended results and introduction to  
1382 the methodologies used in present work.

1383 Supplementary File 1, a zipped folder with the generic prostate model in several formats:  
1384 MaBoSS, GINsim, SBML, as well as images of the networks and their annotations.

1385 Supplementary File 2, a jupyter notebook to inspect Boolean models using MaBoSS. This  
1386 notebook can be used as source code with the model files from Supplementary File 1 to  
1387 generate Figure 3.

1388 Supplementary File 3, a zipped folder with the TCGA-specific personalised models and their  
1389 *Apoptosis* and *Proliferation* phenotype scores.

1390 Supplementary File 4, a TSV file with all the phenotype scores, including *Apoptosis* and  
1391 *Proliferation*, of the TCGA-patient-specific mutations. In the mutation list “\_oe” stands for an  
1392 overexpressed gene and “\_ko” for a knocked out gene.

1393 Supplementary File 5, a zipped folder with the cell-lines-specific personalised models.

1394 Supplementary File 6, a TSV file with all the phenotype scores, including *Apoptosis* and  
1395 *Proliferation*, of all 32258 LNCaP-cell-line-specific mutations and the wild type LNCaP  
1396 model. In the mutation list “\_oe” stands for an overexpressed gene and “\_ko” for a knocked  
1397 out gene.

1398 Supplementary File 7, a spreadsheet with the Key Resources Table of this work.

1399 Source code 1, file needed to obtain Figure 4. Processed datasets needed are Source data  
1400 1 and 2 and are located in the corresponding folder of the repository:  
1401 [https://github.com/ArnauMontagud/PROFILE\\_v2/tree/main/Analysis%20of%20TCGA%20patients%20simulations](https://github.com/ArnauMontagud/PROFILE_v2/tree/main/Analysis%20of%20TCGA%20patients%20simulations)

1402

1403 Source code 2, file needed to perform the drug dosage experiments and obtain Figure 5  
1404 from the main text and Figures 27 and 34-39 from Appendix 1. Processed datasets needed  
1405 is Source data 3 and is located in the corresponding folder of the repository:  
1406 [https://github.com/ArnauMontagud/PROFILE\\_v2/tree/main/Gradient%20inhibition%20of%20nodes](https://github.com/ArnauMontagud/PROFILE_v2/tree/main/Gradient%20inhibition%20of%20nodes)

1407

1408 Source code 3, file needed to obtain Figure 6. Processed datasets needed are Source data  
1409 4 and 5 and are located in the corresponding folder of the repository:  
1410 [https://github.com/ArnauMontagud/PROFILE\\_v2/tree/main/Analysis%20of%20drug%20sensitivities%20across%20cell%20lines](https://github.com/ArnauMontagud/PROFILE_v2/tree/main/Analysis%20of%20drug%20sensitivities%20across%20cell%20lines)

1411

1412 Source code 4, file needed to obtain Figures 7, 8 and 9. Processed datasets needed are  
1413 Source data 6, 7 and 8 and are located in the corresponding folder of the repository:  
1414 [https://github.com/ArnauMontagud/PROFILE\\_v2/tree/main/Analysis%20of%20experimental%20validation](https://github.com/ArnauMontagud/PROFILE_v2/tree/main/Analysis%20of%20experimental%20validation)

1415

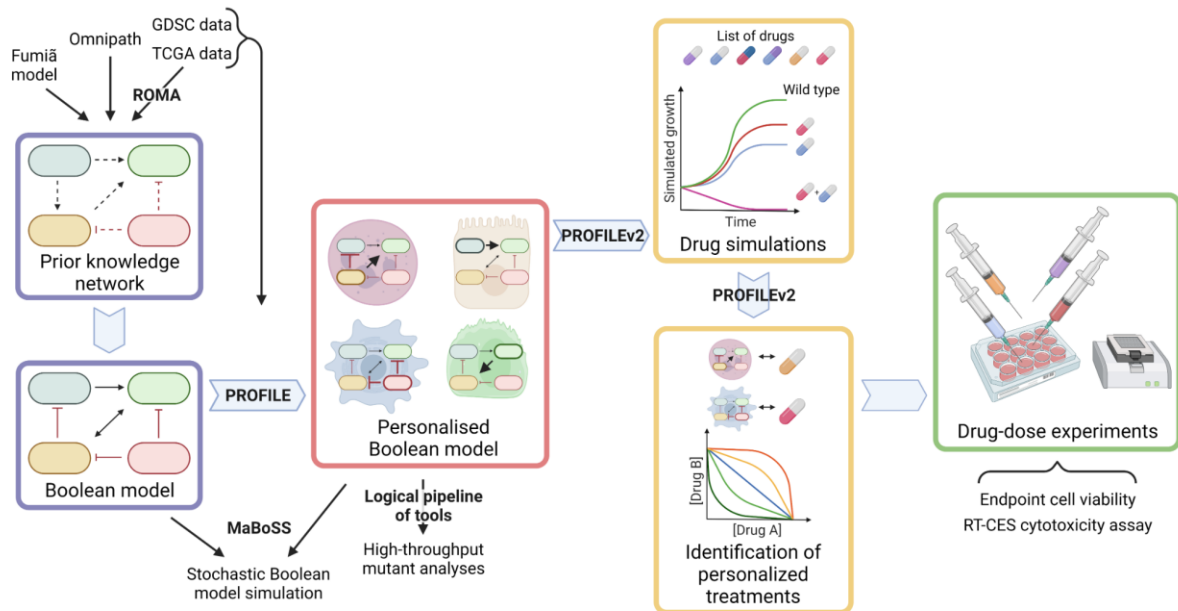
1416

1417

1418

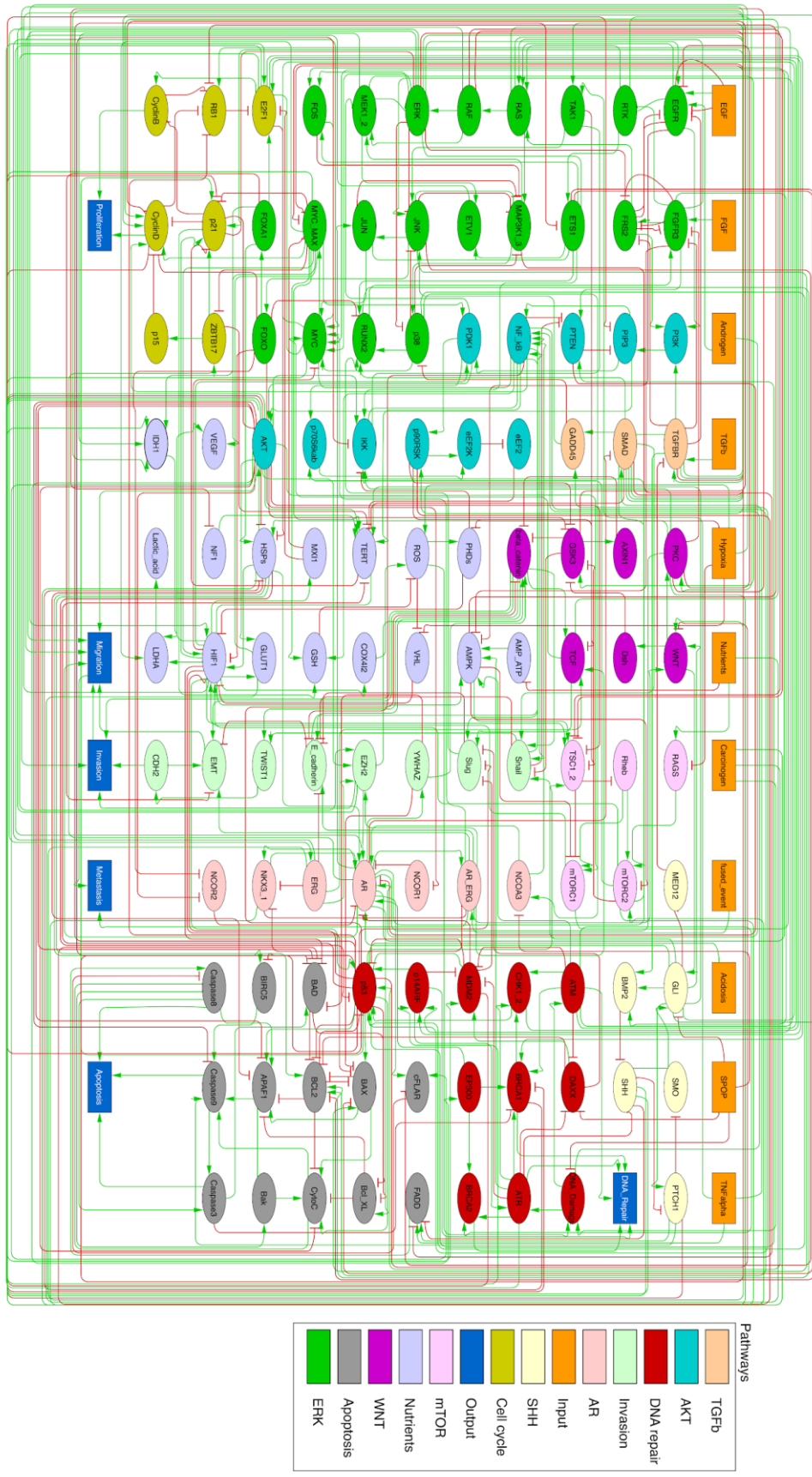
1419 Figures

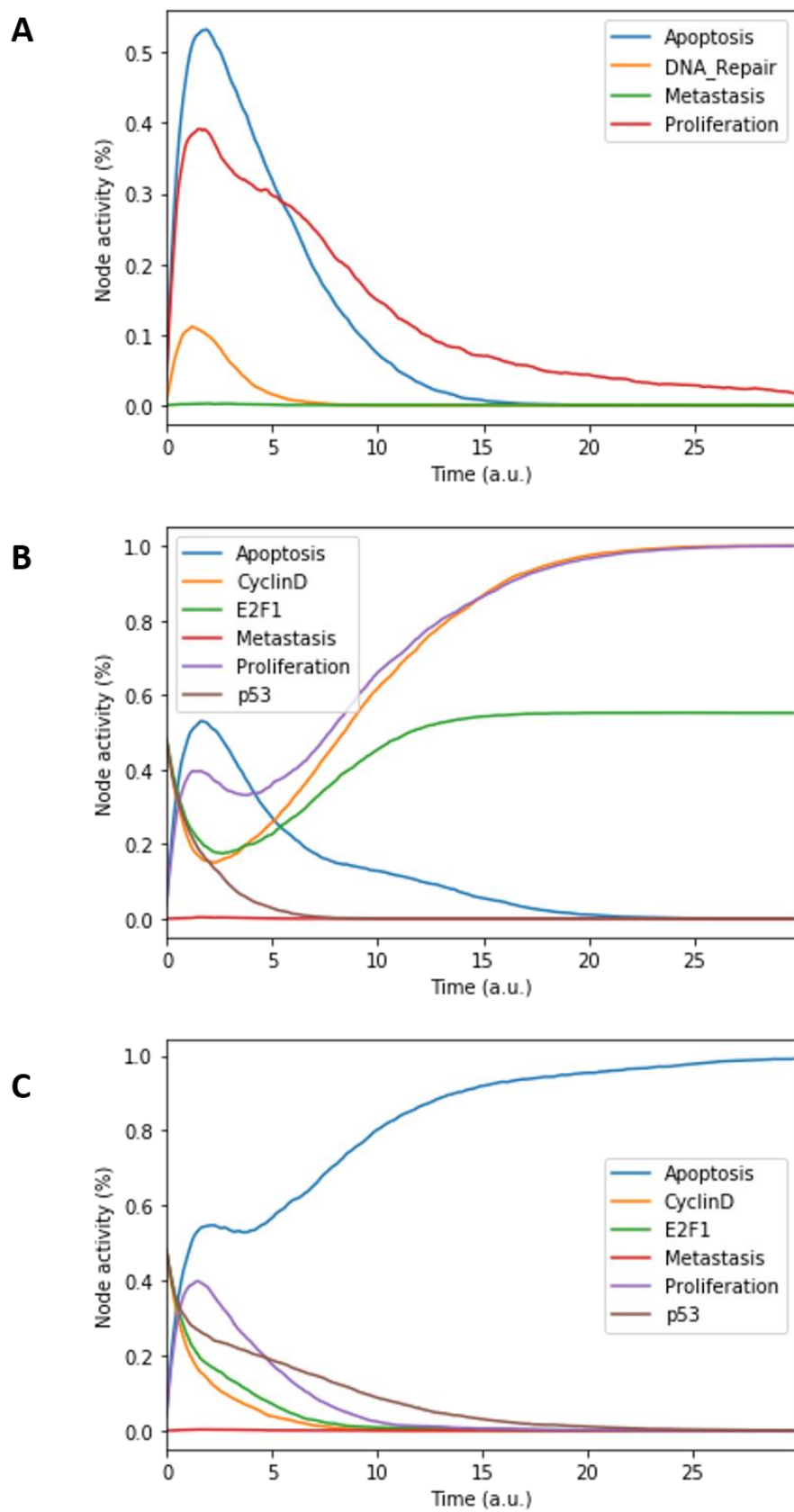
1420



1421

1422 **Figure 1: Workflow to build patient-specific Boolean models and to uncover personalised drug**  
1423 **treatments from present work.**



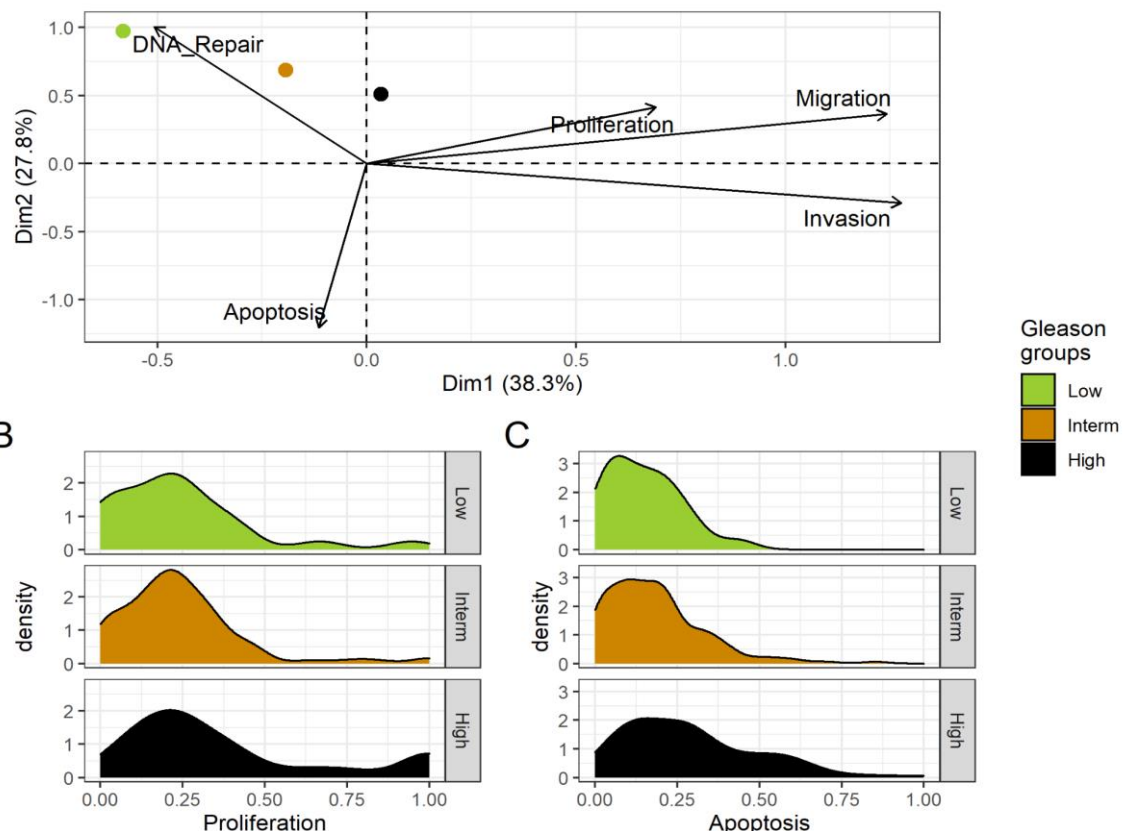


1426

1427

Figure 3: Prostate Boolean model MaBoSS simulations.

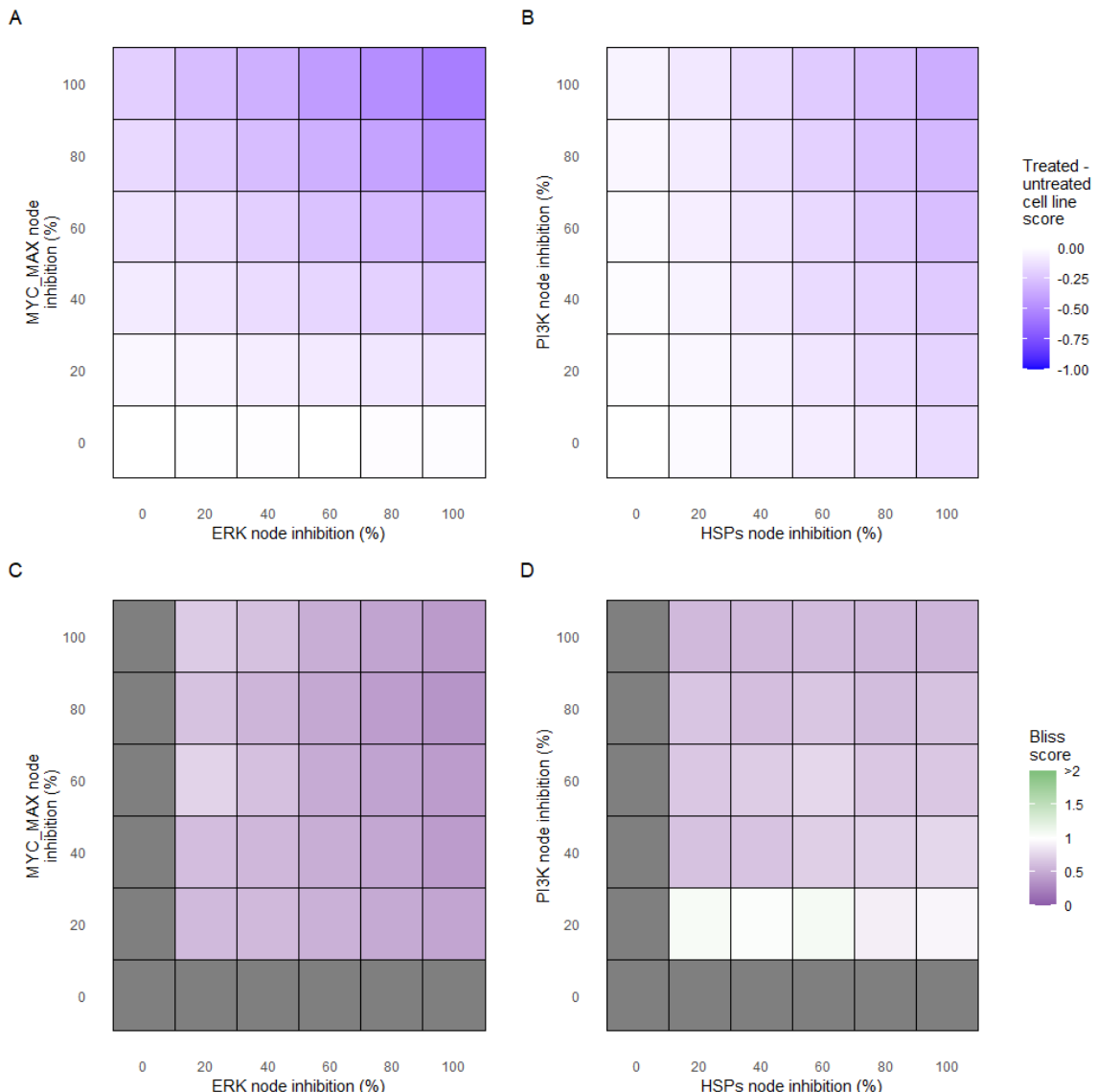
A



1428

1429

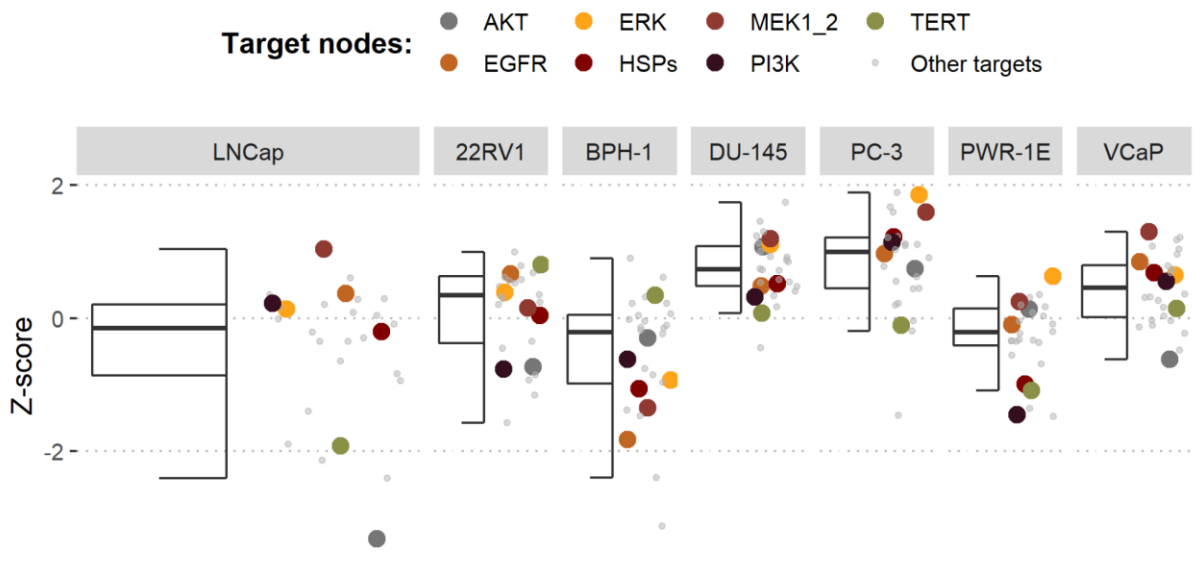
**Figure 4: Associations between simulations and Gleason grades (GG).**



1430

1431      **Figure 5: Phenotype score variations and synergy upon combined ERK and MYC\_MAX (A and**

1432            C) and HSPs and PI3K (B and D) inhibition under EGF growth condition.



1433

1434

**Figure 6: Model-targeting drugs' sensitivities across prostate cell lines.**

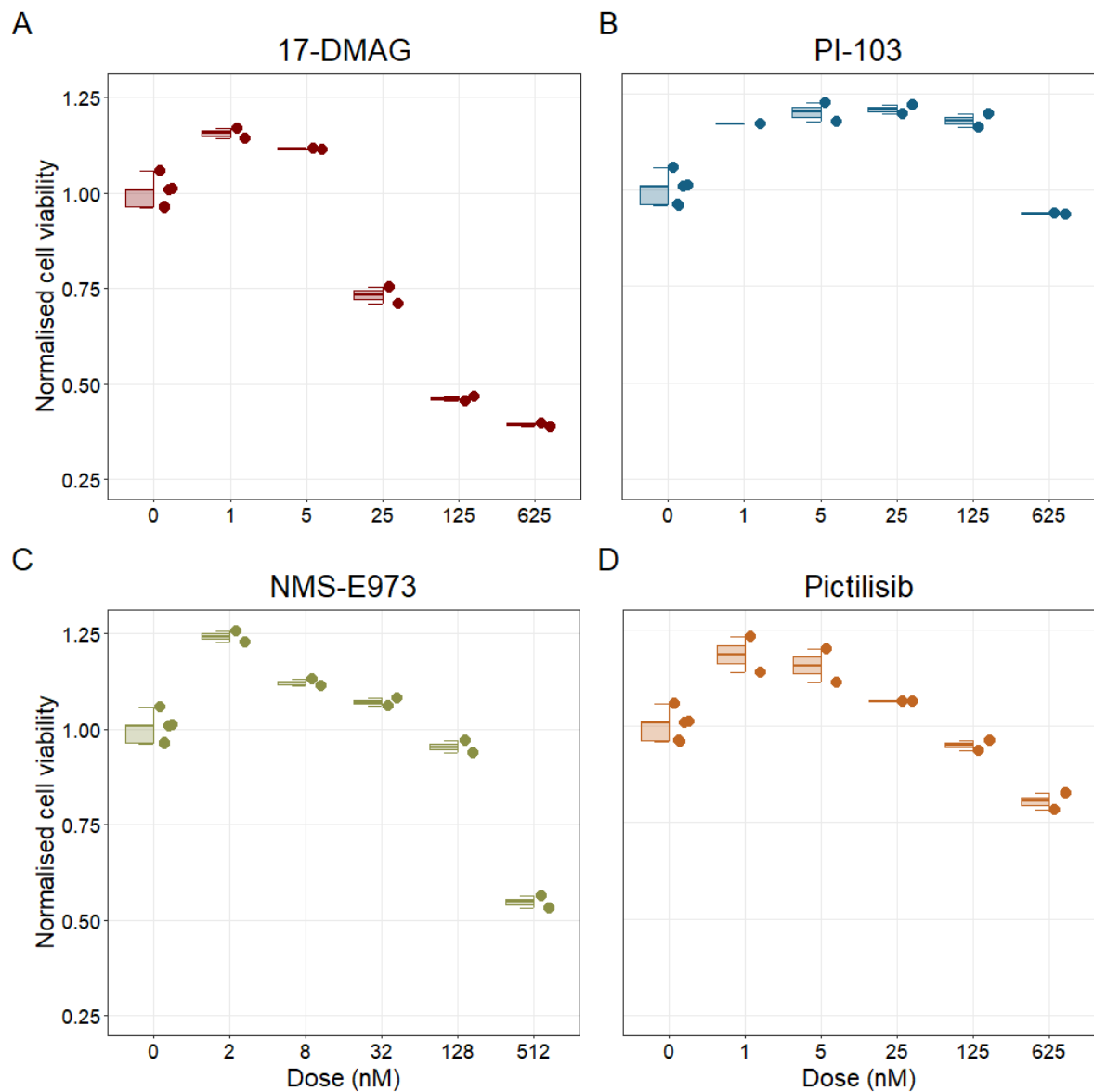
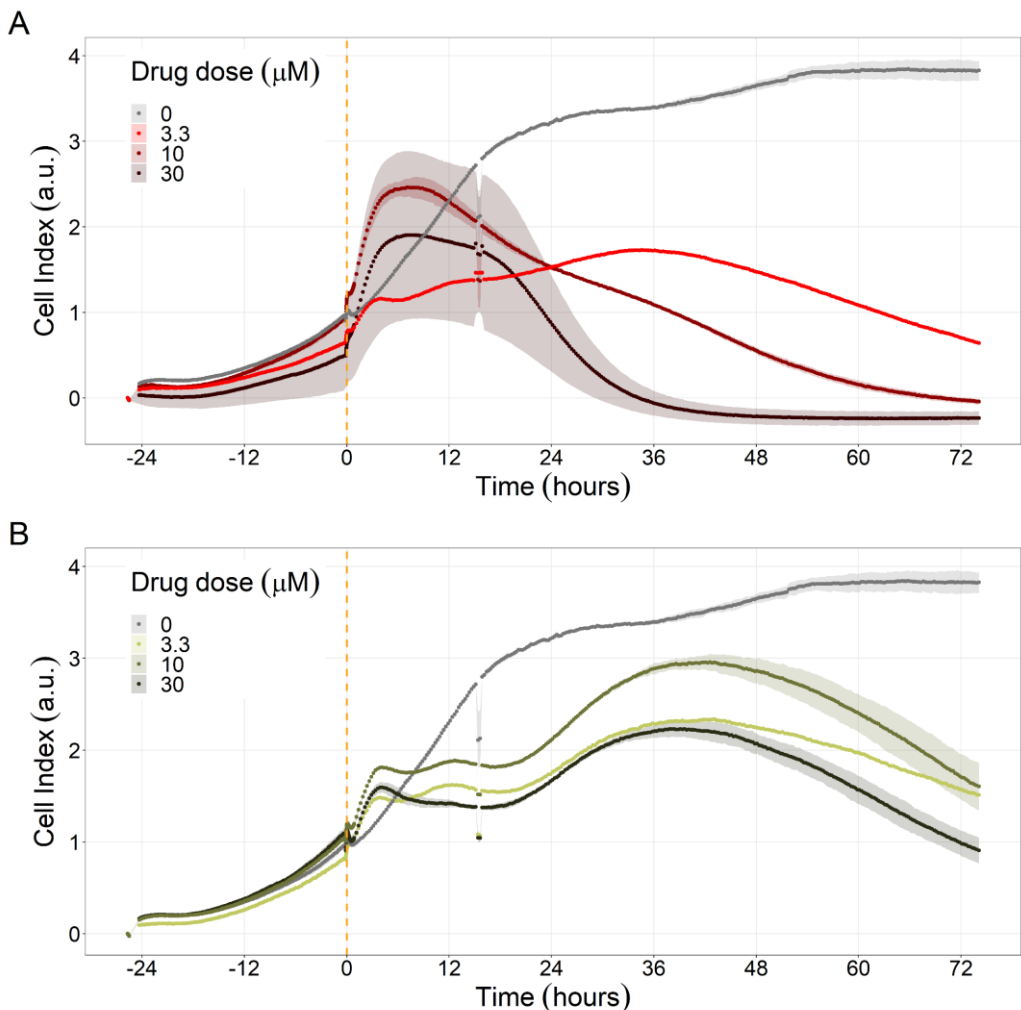


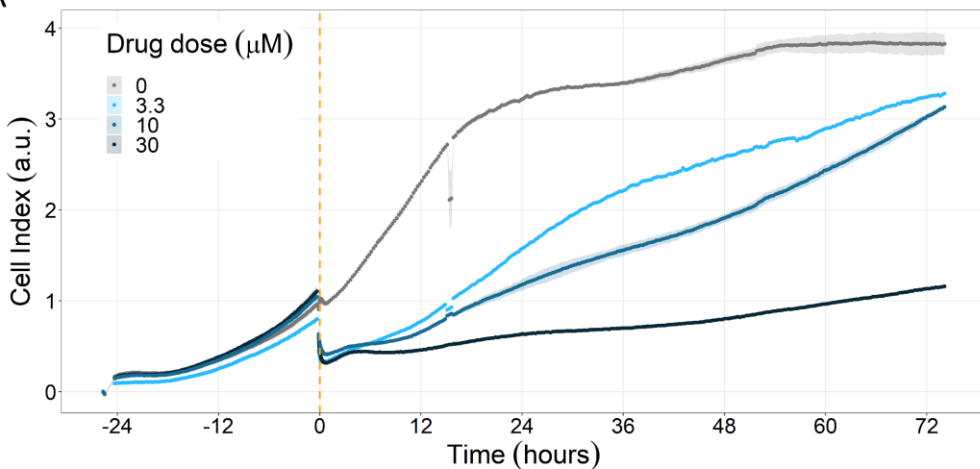
**Figure 7: Cell viability assay determined by the fluorescent resazurin after a 48-hours incubation showed a dose-dependent response to different inhibitors.**



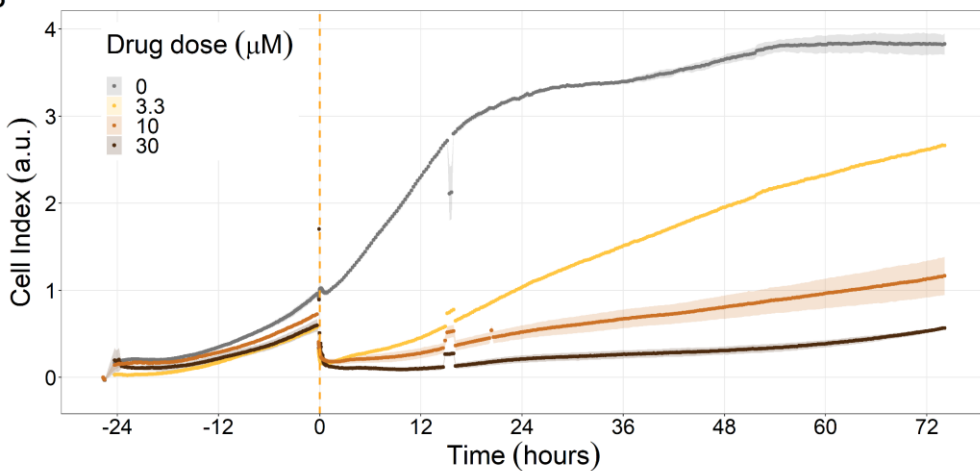
1438  
1439

**Figure 8: Hsp90 inhibitors resulted in dose-dependent changes in the LNCaP cell line growth.**

A



B



1440

1441      **Figure 9: PI3K/AKT pathway inhibition with different PI3K/AKT inhibitors shows the dose-  
1442      dependent response in LNCaP cell line growth.**

1443